

# Testing bath correlation functions for open quantum dynamics simulations

Masaaki Tokieda\*

Department of Chemistry, Graduate School of Science, Kyoto University, Kyoto, Japan

Accurate simulations of thermalization in open quantum systems require a reliable representation of the bath correlation function (BCF). Numerical approaches, such as the hierarchical equations of motion and the pseudomode method, inherently approximate the BCF using a finite set of functions, which can impact simulation accuracy. In this work, we propose a practical and rigorous testing framework to assess the validity of approximate BCFs in open quantum dynamics simulations. Our approach employs a harmonic oscillator system, where the dynamics can be benchmarked against known exact solutions. To enable practical testing, we make two key methodological advancements. First, we develop numerical techniques to evaluate these exact solutions efficiently across a wide range of BCFs for broad applicability. Second, we introduce a moment-based state representation that significantly simplifies computations by exploiting the Gaussian nature of the system. Application to a two-spin system demonstrates that our testing procedure yields reliable error estimates for thermalization simulations. Using this methodology, we assess the performance of recently proposed BCF construction methods, highlighting both their strengths and a notable challenge posed by sub-Ohmic spectral densities at finite temperatures.

## I. INTRODUCTION

Open quantum dynamics describe the evolution of a quantum system interacting with its environment. Simulations of such dynamics serve various purposes. One key objective, central focus of this article, is to provide a dynamical description of thermalization. In the context of open quantum dynamics, thermalization refers to the relaxation of the open system toward a unique steady state corresponding to the reduced Gibbs state when coupled to a thermal environment (or heat bath). Accurate descriptions of thermalization are essential for studying non-equilibrium phenomena [1–4] and for advancing quantum thermodynamics [5–9].

The bath oscillator model, in which a collection of harmonic oscillators (the bath) interacts with a system via a linear interaction operator, is widely used to study open quantum dynamics [10–14]. When the bath is initially in a Gaussian state, its influence on the system is entirely characterized by the two-time correlation function of the interaction operator, called the bath correlation function (BCF). The imaginary part of the BCF, which is independent of the bath state, encodes the bath structure, and its Fourier transform defines the spectral density. For a thermal bath, the BCF satisfies the fluctuation-dissipation relation, which is a key ingredient for thermalization as in the classical Brownian motion [15]. Thermalization is generally expected, as supported by studies employing various approximations (see Ref. [16] and references therein), by results for a specific system with general spectral densities [17], and for general systems with a specific spectral density [18], with possible extensions to more general settings [19].

Due to the lack of analytic solutions for most practical systems, numerical simulations are necessary. Several

methods have been established, including Hierarchical Equations Of Motion (HEOM) [2, 20–23], pseudomode method [24–27], Quasi-Adiabatic propagator Path Integral (QuAPI) [28, 29] and its efficient tensor network implementation called Time-Evolving Matrix Product Operator (TEMPO) [30–33], MultiConfiguration Time-Dependent Hartree (MCTDH) [34, 35], the chain mapping technique called Time Evolving Density operator with Orthogonal Polynomials Algorithm (TEDOPA) [36–39], and stochastic methods [40–42]. In this article, we mainly focus on the methods of HEOM and pseudomode, whose connection was recently elucidated in Refs. [43–45]. These methods require approximating the BCF as a finite sum of functions, each corresponding to an auxiliary bosonic mode. Intuitively, one can view the system as being coupled to a finite set of dissipative auxiliary modes, whose structure is engineered to reproduce the bath influences encoded in the BCF. While reducing the number of auxiliary modes is desirable for computational efficiency, an inaccurate BCF leads to unreliable results. In particular, failure to satisfy the fluctuation-dissipation relation can lead to poor reproduction of the thermalization behavior. Such issues become increasingly severe for more complex BCFs, which are gaining attention as more realistic models of physical environments [46–49].

While the error in an approximated BCF can be readily estimated, evaluating its impact on simulation results is nontrivial. Previous works Refs. [50, 51] derived upper bounds on the error in expectation values based on the BCF or spectral density error. However, these bounds grow exponentially with time and significantly overestimate the actual error once the system reaches a steady state. Thus, they are unsuitable for assessing the error for thermalization simulations. A more practical approach is to examine convergence with increasing BCF accuracy. Yet, when the BCF or system is complex, other truncation parameters make such calibration difficult, motivating the need for a simpler test.

\*Electronic address: [tokieda.masaaki.4e@kyoto-u.ac.jp](mailto:tokieda.masaaki.4e@kyoto-u.ac.jp)

To this end, we propose replacing the system with a simpler and exactly solvable one, while maintaining the same BCF. We then compare the simulation results with the exact solutions to assess the validity of an approximate BCF. A well-known exactly solvable model is a dephasing model, where the system and interaction Hamiltonians commute [52]. However, this model does not thermalize due to the presence of conserved quantities. As an alternative, we consider a harmonic oscillator system, which admits exact solutions and is known to thermalize for general spectral densities [17]. In Ref. [53], non-Markovian tests were introduced to assess the accuracy of numerical methods using this system (see also Ref. [54]). Here, we use them to test the BCF. Thus far, the applications of non-Markovian tests have been limited to simple spectral densities, where exact solutions can readily be obtained. We also note that the infinite-dimensional nature of the oscillator Hilbert space poses computational challenges and introduces another source of error due to the truncation of the system state.

To enable practical testing, this work offers two key contributions. First, we revisit the exact solutions in Ref. [17] and develop efficient numerical evaluation methods, extending their applicability to general spectral densities. Second, we introduce a system state representation based on ladder operator moments [43, 45]. Owing to the Gaussian nature of the total system, both system and auxiliary states can be exactly truncated at low orders in this representation. Compared to other state representations (e.g., Fock basis or Wigner function), this approach simplifies the testing procedure by reducing computational costs and eliminating the need to calibrate truncation levels. In this regard, we note that the use of the harmonic oscillator system is advantageous over the dephasing model, which requires truncating auxiliary states.

The remainder of this article is organized as follows. In Sec. II, we describe the testing methodologies. In Sec. III, we compare the performance of recently proposed algorithms for efficiently constructing approximate BCFs. In Sec. IV, we demonstrate the test procedure using a two-spin system and show its effectiveness. Finally, Sec. V provides summaries and concluding remarks.

## II. METHODOLOGIES

### A. Bath oscillator model

We consider open quantum dynamics described by a bath oscillator model. The evolution of the total density operator,  $\rho_{\text{tot}}$ , is governed by

$$\frac{d}{dt}\rho_{\text{tot}}(t) = -\frac{i}{\hbar}[H_{\text{tot}}, \rho_{\text{tot}}(t)]$$

with

$$H_{\text{tot}} = H_S + \sum_m \hbar\omega_m b_m^\dagger b_m + V_S \sum_m u_m (b_m + b_m^\dagger). \quad (1)$$

In this model, the bath consists of harmonic oscillators with annihilation (creation) operators  $b_m$  ( $b_m^\dagger$ ) for the  $m$ -th mode obeying the bosonic commutation relations  $[b_m, b_n^\dagger] = \delta_{m,n}$ , with the Kronecker delta  $\delta_{m,n}$ . Each mode has a frequency  $\omega_m$  and couples to the system with strength  $u_m$ . We define the bath Hamiltonian and interaction operator as  $H_B \equiv \sum_m \hbar\omega_m b_m^\dagger b_m$  and  $X_B \equiv \sum_m u_m (b_m + b_m^\dagger)$ . The Hermitian operators  $H_S$  and  $V_S$  describe the system's internal dynamics and its interaction with the bath, respectively. The bath interaction modifies the bare potential in  $H_S$ , which can be compensated by introducing a counter term [12]

$$H_S = H_{S,\text{eff}} + \lambda V_S^2, \quad (2)$$

with the effective system Hamiltonian  $H_{S,\text{eff}}$  and  $\lambda = \sum_m u_m^2 / (\hbar\omega_m)$ .

We focus on the evolution of the system's reduced density operator, defined as  $\rho_S(t) \equiv \text{tr}_B[\rho_{\text{tot}}(t)]$ , where  $\text{tr}_B$  denotes the trace over the bath. Assuming an initially uncorrelated state  $\rho_{\text{tot}}(0) = \rho_S(0)\rho_B$  with a thermal bath  $\rho_B = \exp(-\beta H_B) / \text{tr}_B[\exp(-\beta H_B)]$ , where  $\beta$  is the inverse temperature, the evolution of  $\rho_S(t)$  is given by [10]

$$\rho_S(t) = e^{-iH_S^\times t/\hbar} \mathcal{T}[\mathcal{M}(t)] \rho_S(0), \quad (3)$$

with the propagator

$$\mathcal{M}(t) = \exp \left[ -\frac{1}{\hbar} \int_0^t ds \int_0^s du \right. \\ \left. V_S^I(s)^\times \{L(s-u)V_S^I(u)^L - L^*(s-u)V_S^I(u)^R\} \right], \quad (4)$$

where we introduce the chronological time-ordering  $\mathcal{T}$ , the superoperator notations  $o^\times \rho = [o, \rho]$ ,  $o^L \rho = o\rho$ ,  $o^R \rho = \rho o$  for any operators  $\rho$  and  $o$ ,  $V_S^I(t) = \exp(iH_S^\times t/\hbar)V_S$ , and the BCF  $L(t)$  defined by

$$L(t) \equiv \frac{1}{\hbar} \text{tr}_B[e^{iH_B^\times t/\hbar}(X_B)X_B \rho_B] \\ = \int_0^\infty \frac{d\omega}{\pi} J(\omega) \left[ \coth \left( \frac{\beta\hbar\omega}{2} \right) \cos(\omega t) - i \sin(\omega t) \right], \quad (5)$$

with  $J(\omega) = (\pi/\hbar) \sum_m u_m^2 [\delta(\omega - \omega_m) - \delta(\omega + \omega_m)]$  the spectral density. To model irreversible dynamics, we consider a smooth spectral density  $J(\omega)$  representing continuously distributed bath modes.

### B. HEOM and pseudomode

To compute Eq. (3) numerically, we employ the methods of HEOM and pseudomode. We begin by deriving the HEOM following Ref. [55]. This involves considering a model BCF  $L_{\text{mod}}(t)$  expressed with  $K$  (generally complex) basis functions  $\{v_k(t)\}_{k=1}^K$  as

$$L_{\text{mod}}(t \geq 0) = \sum_{k=1}^K d_k v_k(t) \equiv \mathbf{d}^\top \mathbf{v}(t), \quad (6)$$

where  $d_k$  ( $k = 1, \dots, K$ ) are complex numbers and  $\top$  denotes the matrix transpose. We impose the following three assumptions on the set  $\{v_k(t)\}_{k=1}^K$ . First, the vector  $\mathbf{v}(t)$  is closed under time differentiation as  $(d/dt)\mathbf{v}(t) = -Z\mathbf{v}(t)$  for some  $K \times K$  complex matrix  $Z$ . Second, the set  $\{v_k(t)\}_{k=1}^K$  is closed under complex conjugation, namely, there exists a complex vector  $\bar{\mathbf{d}}^\top = [\bar{d}_1, \dots, \bar{d}_K]$  such that  $(\mathbf{d}^\top \mathbf{v}(t))^* = \bar{\mathbf{d}}^\top \mathbf{v}(t)$ . Third, there exist a complex vector  $\boldsymbol{\theta} \in \mathbb{C}^K$  and  $K \times K$  complex matrices  $D$  and  $\bar{D}$  such that  $\mathbf{d}^\top = \boldsymbol{\theta}^\top D$ ,  $\bar{\mathbf{d}}^\top = \boldsymbol{\theta}^\top \bar{D}$ , and  $[D, Z] = [\bar{D}, Z] = 0$ .

Under the last two assumptions, the propagator Eq. (4) with  $L_{\text{mod}}(t)$  can be expressed as

$$\mathcal{M}(t) = \exp \left[ -\frac{1}{\hbar} \int_0^t ds V_S^I(s)^\times \sum_{k=1}^K \theta_k \mathcal{Y}_k(s) \right],$$

with

$$\mathcal{Y}_k(s) = \int_0^s du ([D \mathbf{v}(s-u)]_k V_S^I(u)^L - [\bar{D} \mathbf{v}(s-u)]_k V_S^I(u)^R).$$

To obtain the evolution of  $\rho_S(t)$ , we calculate the time derivative of  $\mathcal{T}[\mathcal{M}(t)]$ :

$$\frac{d}{dt} \mathcal{T}[\mathcal{M}(t)] = -\frac{1}{\hbar} V_S^I(t)^\times \mathcal{T} \left[ \sum_{k=1}^K \theta_k \mathcal{Y}_k(t) \mathcal{M}(t) \right].$$

Since the latest time in  $\mathcal{T}$  is  $t$ ,  $V_S^I(t)^\times$  can be taken outside the time-ordering. In contrast,  $\mathcal{Y}_k(t)$  includes superoperators evaluated at earlier times  $s < t$  and must remain inside. To obtain closed differential equations, we introduce the following auxiliary system operators:

$$\rho_{\mathbf{j}}(t) = e^{-iH_S^\times t/\hbar} \mathcal{T} \left[ \prod_{k=1}^K \left\{ \frac{(\mathcal{Y}_k(t))^{j_k}}{\sqrt{j_k!}} \right\} \mathcal{M}(t) \right] \rho_S(0), \quad (7)$$

with  $\mathbf{j}^\top = [j_1, \dots, j_K]$  and  $j_k \in \mathbb{Z}_{\geq 0}$  ( $k = 1, \dots, K$ ). Note that the reduced density operator corresponds to the element with  $\mathbf{j} = \mathbf{0}$ :  $\rho_{\mathbf{0}}(t) = \rho_S(t)$  [see Eq. (3)]. These yield HEOM

$$\begin{aligned} \frac{d}{dt} \rho_{\mathbf{j}}(t) &= -\frac{i}{\hbar} H_S^\times \rho_{\mathbf{j}}(t) - \sum_{k,k'=1}^K Z_{k,k'}^{\mathbf{j}} \rho_{\mathbf{j}-\mathbf{e}_k+\mathbf{e}_{k'}}(t) \\ &+ \sum_{k=1}^K \sqrt{j_k} ([D \mathbf{v}(0)]_k V_S^L - [\bar{D} \mathbf{v}(0)]_k V_S^R) \rho_{\mathbf{j}-\mathbf{e}_k}(t) \quad (8) \\ &- \frac{1}{\hbar} \sum_{k=1}^K \theta_k \sqrt{j_k + 1} V_S^\times \rho_{\mathbf{j}+\mathbf{e}_k}, \end{aligned}$$

where  $\mathbf{e}_k$  are  $K$ -dimensional unit vectors with  $[\mathbf{e}_k]_l = \delta_{k,l}$  and  $Z_{k,k'}^{\mathbf{j}} = Z_{k,k'} \sqrt{j_k(j_{k'} + 1 - \delta_{k,k'})}$ .

From Eq. (7), the initial conditions are  $\rho_{\mathbf{0}}(0) = \rho_S(0)$  and  $\rho_{\mathbf{j} \neq \mathbf{0}}(0) = 0$ . Solving Eq. (8) under these conditions

yields the reduced density operator from the  $\mathbf{j} = \mathbf{0}$  element. Since the HEOM Eq. (8) is a system of infinitely many coupled differential equations for  $\rho_{\mathbf{j}}(t)$  ( $\forall \mathbf{j} \in \mathbb{Z}_{\geq 0}^K$ ), truncation is necessary for numerical computation. A common strategy is to limit the hierarchy depth  $\sum_{k=1}^K j_k$  to a finite cutoff  $H$ , resulting in  $(H+K)!/(H!K!)$  coupled equations for  $\rho_{\mathbf{j}}(t)$  with  $\sum_{k=1}^K j_k \leq H$  [23, 56]. Minimizing  $K$  while preserving the accuracy of  $L_{\text{mod}}(t)$  is therefore crucial for computational efficiency.

Recent results Refs. [43–45] have revealed a close connection between the pseudomode method and the HEOM. The key difference lies in how the auxiliary states are represented: while the pseudomode method uses a direct representation, HEOM expresses these states in terms of ladder operator moments. This representational difference, central to the discussion in Sec. II D, is exemplified in Appendix A, where we show that a pseudomode equation can be recast into a special case of the HEOM Eq. (8). Therefore, it suffices to use Eq. (8) for a unified treatment of both methods.

### C. Testing $L_{\text{mod}}(t)$

BCFs defined as Eq. (5) cannot be exactly represented as Eq. (6) with finite  $K$ , implying an inherent error in the model BCF. To assess its impact on the dynamics, we consider a surrogate harmonic oscillator system [see Eq. (2)]:

$$\begin{aligned} H_{S,\text{eff}} &= \hbar \omega_0 a^\dagger a, \\ V_S &= v_0 q, \end{aligned} \quad (9)$$

with the annihilation (creation) operator  $a$  ( $a^\dagger$ ) satisfying  $[a, a^\dagger] = 1$ ,  $q = (a + a^\dagger)/\sqrt{2}$ , the frequency  $\omega_0$ , and the coupling parameter  $v_0$ .

This system is well-suited for benchmarking, as the quadratic form of the total Hamiltonian permits exact solutions. For example, the Heisenberg equations of motion for the system operators can be solved analytically as shown in Appendix B 1. The evolution is governed by a kernel function  $G_+(t)$  [see Eq. (B1)], which is the solution of the integro-differential equation

$$\frac{d^2}{dt^2} G_+(t) + \frac{\omega_0 v_0^2}{\hbar} \int_0^t ds \eta(t-s) \frac{d}{ds} G_+(s) + \omega_0^2 q(t) = 0,$$

with initial conditions  $G_+(0) = 0$  and  $(d/dt)G_+(0) = 1$ . Here,  $\eta(t)$  is the friction kernel, defined by

$$\eta(t) \equiv 2 \int_0^\infty \frac{d\omega}{\pi} \frac{J(\omega)}{\omega} \cos(\omega t),$$

which relates to the imaginary part of the BCF as  $2\text{Im}[L(t)] = (d/dt)\eta(t)$ , where  $\text{Im}$  denotes the imaginary part. Beyond solvability, this system exhibits thermalization: if  $G_+(t)$  decays sufficiently fast, then  $\lim_{t \rightarrow \infty} \rho_S(t) = \text{tr}_B[\exp(-\beta H_{\text{tot}})]/\text{tr}[\exp(-\beta H_{\text{tot}})]$

holds, with  $\text{tr}$  the trace over the total space, independent of the initial state  $\rho_S(0)$  [17].

We denote the equilibrium expectation value of an operator  $o$  as  $\langle o \rangle_{\text{eq}} = \text{tr}[o \exp(-\beta H_{\text{tot}})] / \text{tr}[\exp(-\beta H_{\text{tot}})]$ . Following the non-Markovian tests [53, 54], for  $o = q$  and  $o = p \equiv i(a^\dagger - a)/\sqrt{2}$ , we focus on the equilibrium expectation values of  $o^2$ ,  $\langle o^2 \rangle_{\text{eq}}$ , and the equilibrium autocorrelation functions,  $C_{oo}(t) \equiv \langle \exp(iH_{\text{tot}}^\times t/\hbar)(o) o \rangle_{\text{eq}}$ , in the frequency domain

$$\mathcal{F}[C_{oo}](\omega) \equiv \int_{-\infty}^{\infty} dt C_{oo}(t) e^{i\omega t}.$$

Note  $\mathcal{F}[C_{oo}](\omega) = 2\text{Re}[\int_0^\infty dt C_{oo}(t) \exp(i\omega t)]$  due to  $C_{oo}(-t) = [C_{oo}(t)]^*$ . Although the original tests included computing higher-order correlation functions [53], we restrict our analysis to second-order ones, as the Gaussianity ensures that higher-order correlations are entirely determined by them.

As shown in Ref. [17], analytic expressions for these quantities are available and presented explicitly in Appendix B 2. A key observation is that their evaluation requires only the Laplace transform of the friction kernel,

$$\hat{\eta}(s) = \int_0^\infty dt \eta(t) e^{-st} \quad (\text{Re}(s) \geq 0),$$

where  $\text{Re}$  denotes the real part. Inserting the definition of  $\eta(t)$ ,  $\hat{\eta}(s)$  can be expressed with  $J(\omega)$  as

$$\hat{\eta}(s) = \frac{2s}{\pi} \int_0^\infty d\omega' \frac{J(\omega')/\omega'}{(\omega')^2 + s^2}. \quad (10)$$

Specifically, we require  $\hat{\eta}(|s|)$  ( $|s| > 0$ ) for computing  $\langle o^2 \rangle_{\text{eq}}$  and  $\hat{\eta}(-i\omega)$  ( $\omega \in \mathbb{R}$ ) for  $C_{oo}(t)$  ( $o = q$  and  $p$ ).

In Appendix B 3, we present analytic expressions for  $\hat{\eta}(s)$  in several cases. When such expressions are unavailable, numerical evaluation is required. For  $\hat{\eta}(|s|)$  ( $|s| > 0$ ), the integral in Eq. (10) can be computed directly. For  $\hat{\eta}(-i\omega)$  ( $\omega \in \mathbb{R}$ ), on the other hand, the integrand has a pole at  $\omega' = |\omega|$ . By deforming the contour to avoid the pole, we obtain

$$\hat{\eta}(-i\omega) = \frac{J(\omega)}{\omega} - i \frac{2\omega}{\pi} \text{p.v.} \int_0^\infty d\omega' \frac{J(\omega')/\omega'}{(\omega')^2 - \omega^2}, \quad (11)$$

where  $\text{p.v.}$  denotes the Cauchy principal value. This expression is amenable to numerical evaluation and also provides analytic insight into the behavior of  $\mathcal{F}[C_{qq}](\omega)$  near  $\omega = 0$  [see Eq. (B3)].

An alternative way to evaluate  $\hat{\eta}(s)$  is to fit the spectral density  $J(\omega)$  using simple functions. A promising approach is to approximate  $\text{Im}[L(t)]$  or  $\eta(t)$  by a finite (though possibly large) sum of complex exponentials:

$$\begin{aligned} \text{Im}[L(t \geq 0)] &= -2 \sum_j \text{Im}[c_j e^{-\mu_j t}] \quad \text{or} \\ \eta(t \geq 0) &= 4 \sum_j \text{Im}[(c_j/\mu_j) e^{-\mu_j t}], \end{aligned} \quad (12)$$

where  $\{c_j, \mu_j\}_j$  are complex fitting parameters with  $\text{Re}(\mu_j) > 0$  for the stability. The corresponding spectral density  $J(\omega)$  follows from the Fourier transform [see Eq. (C1)]. If  $\text{Im}(c_j) = 0$  is assumed,  $J(\omega)$  is given by

$$J(\omega) = \sum_j \frac{p_j \omega}{[(\omega + \Omega_j)^2 + \Gamma_j^2] \cdot [(\omega - \Omega_j)^2 + \Gamma_j^2]}, \quad (13)$$

with  $\Gamma_j = \text{Re}(\mu_j)$ ,  $\Omega_j = \text{Im}(\mu_j)$ , and  $p_j = 8\text{Re}(c_j)\Omega_j\Gamma_j$ . This decomposition was originally proposed by Meier and Tannor [57], and Eq. (12) serves as its generalization. In Appendix C, we explore this model in more detail, including a fitting procedure. Given  $\{c_j, \mu_j\}_j$ , the analytic expression for  $\hat{\eta}(s)$  valid for  $\text{Re}(s) \geq 0$  is available [see Eq. (B4)], enabling evaluation of the exact solutions.

In summary, we presented practical methods to evaluate  $\hat{\eta}(s)$  for  $\text{Re}(s) \geq 0$ , extending exact solutions to a broader class of spectral densities.

#### D. Moment representation of the oscillator state

Previous non-Markovian tests [53, 54] solved the quantum Fokker-Planck equation, which is the Wigner representation of the HEOM Eq. (8). Alternatively, the conventional Fock basis can be used to represent the oscillator system state. Since the oscillator Hilbert space is infinite-dimensional, truncation is necessary for numerical computations. Under strong system-bath coupling, both the effective system dimension and the required hierarchy depth increase, limiting the applicability of these approaches to simple cases with small  $K$  (the number of terms in  $L_{\text{mod}}(t)$ ). Additionally, truncating the oscillator state introduces another source of error, obscuring whether deviations in the results stem from  $L_{\text{mod}}(t)$  or the state truncation.

To address these issues, we adopt the moment representation of the oscillator state:

$$\phi_{m,n,j}(t) \equiv \frac{\text{tr}_S(a^m \rho_j(t) (a^\dagger)^n)}{\sqrt{m! n!}}, \quad (14)$$

where  $\text{tr}_S$  denotes the trace over the system. For  $j = 0$ , the set  $\{\phi_{m,n,0}(t)\}_{m,n=0}^\infty$  corresponds to the moments of the ladder operators. A detailed discussion of this representation is provided in Appendix D. In Appendix D 2, we derive the evolution equation for  $\{\phi_{m,n,j}(t)\}$ , namely the HEOM Eq. (8) in this representation. This reveals that the evolution of each element  $\phi_{m,n,j}(t)$ , with depth  $\mathcal{H} \equiv m + n + \sum_{k=1}^K j_k$ , depends only on elements with depth  $\mathcal{H}$  or  $\mathcal{H} - 2$ . This decoupling follows from the use of the moment representation for the auxiliary states in HEOM, as discussed at the end of Sec. II B, and the Gaussian nature of the total system.

This decoupling enables exact truncation in the moment representation. For example,  $\langle o^2 \rangle_{\text{eq}}$  and  $\mathcal{F}[C_{oo}](\omega)$  for  $o = q$  and  $p$  are second-order moments, and their computation only require elements  $\{\phi_{m,n,j}\}$  with  $m+n+\sum_{k=1}^K j_k \leq 2$ . This set contains only  $(K+4)!/(2!(K+2)!)$

complex numbers, allowing efficient computation of the dynamics even for large  $K$ . Moreover, since the truncation is exact, we can isolate and assess the impact of the approximation in  $L_{\text{mod}}(t)$ , enabling reliable testing.

### III. ACCURACY ANALYSIS

In this section, we apply the methodologies developed in the previous section to concrete examples. Throughout this section, we model the BCF as a linear combination of exponential functions:

$$L_{\text{mod}}(t \geq 0) = \sum_{k=1}^K d_k e^{-z_k t}, \quad (15)$$

or equivalently  $v_k(t) = \exp(-z_k t)$  in Eq. (6), where  $z_k \in \mathbb{C}$  with  $\text{Re}(z_k) > 0$  for stability. To conform to the assumptions in Sec. IIIB, we take the set  $\{z_k\}_{k=1}^K$  to be closed under complex conjugation. The matrix  $Z$  is diagonal as  $Z = \text{diag}[z_1 \ z_2 \ \dots \ z_K]$ , indicating that the third assumption can be met by setting  $\boldsymbol{\theta}^\top = [1 \ 1 \ \dots \ 1]$ ,  $D = \text{diag}[d_1 \ d_2 \ \dots \ d_K]$ , and  $\bar{D} = \text{diag}[d_1 \ \bar{d}_2 \ \dots \ \bar{d}_K]$ . The resulting HEOM Eq. (8) reads as

$$\begin{aligned} \frac{d}{dt} \rho_{\mathbf{j}}(t) = & - \left[ \frac{i}{\hbar} H_S^\times + \sum_{k=1}^K z_k j_k \right] \rho_{\mathbf{j}}(t) \\ & + \sum_{k=1}^K \sqrt{j_k} (d_k V_S^L - \bar{d}_k V_S^R) \rho_{\mathbf{j}-\mathbf{e}_k}(t) \\ & - \frac{1}{\hbar} \sum_{k=1}^K \sqrt{j_k + 1} V_S^\times \rho_{\mathbf{j}+\mathbf{e}_k}. \end{aligned} \quad (16)$$

Several methods have recently been proposed to fit the BCF in the form of Eq. (15), as summarized in Sec. IIIA. In Sec. IIIB, we compare their performance. Lastly, in Sec. IIIC, we examine a challenging case involving a sub-Ohmic spectral density and highlight a potential limitation of a method.

#### A. Fitting algorithms

Here we introduce four methods for fitting the BCF in the form of Eq. (15). The following descriptions focus on a broad overview of each method, and technical details are deferred to the cited references and appendices.

(i) *Adaptive Antoulas-Anderson (AAA) algorithm.* The algorithm offers a rational approximation for real or complex functions [58], and was applied in Ref. [59] to fit the Fourier transform of the BCF:

$$\mathcal{F}[L](\omega) = \frac{2J(\omega)}{1 - e^{-\beta\hbar\omega}}. \quad (17)$$

It models the BCF in the barycentric form as

$$\mathcal{F}[L_{\text{mod}}](\omega) = \frac{\sum_j \mathcal{F}[L](\omega_j) W_j / (\omega - \omega_j)}{\sum_j W_j / (\omega - \omega_j)},$$

with the parameters  $\{\omega_j, W_j\}_j$  determined iteratively. A partial fraction decomposition then expresses  $\mathcal{F}[L_{\text{mod}}](\omega)$  as a sum over simple poles, which yields the time-domain expression as Eq. (15).

(ii) *Interacting Pseudomode (IP) approach.* In Refs. [60, 61], the authors fit the Fourier transform of the BCF using the ansatz,

$$\mathcal{F}[L_{\text{mod}}](\omega) = \frac{1}{\pi} \mathbf{l}^\top \text{Im} [(\tilde{\omega} - \omega)^{-1}] \mathbf{l}, \quad (18)$$

where the fitting parameters are a real vector  $\mathbf{l}$  and a complex matrix  $\tilde{\omega}$  with elements  $\tilde{\omega}_{k,k'} = \omega_{k,k'} - (i/2)\delta_{k,k'}\kappa_k$  with a real symmetric  $\omega_{k,k'}$  and positive  $\kappa_k$ .

This form arises from an interacting pseudomode model, as elaborated in Appendix A. Note that we have  $\mathcal{F}[L_{\text{mod}}](\omega) > 0$  for any  $\omega$ , which ensures complete positivity of the reduced dynamics [62]. Diagonalizing  $\tilde{\omega}$  expresses  $\mathcal{F}[L_{\text{mod}}](\omega)$  as a sum over simple poles, leading to the time-domain expression as Eq. (15). We note that this approach has also gained attention for its potential application in quantum algorithms for simulating open quantum dynamics [63, 64].

(iii) *Estimation of Signal Parameters via Rotational Invariance Techniques (ESPRIT).* For equidistant data points  $\{L(t_n)\}_n$  with  $t_n = n\Delta t_{\text{data}}$ , ESPRIT estimates  $\{d_k, z_k\}_{k=1}^K$  by minimizing  $\sum_n |L(t_n) - L_{\text{mod}}(t_n)|$ , using the translational identity  $\exp(-z_k t_m) \exp(-z_k t_n) = \exp(-z_k t_{m+n})$  [65]. Its application to BCF fitting was proposed in Ref. [66], demonstrating superior performance over AAA and other time-domain fitting methods.

(iv) *Generalized Mayer-Tannor with FITted Matsubara modes (GMT&FIT).* In Ref. [67], a two-step approach was proposed. First, the spectral density is fitted using the Maier-Tannor form Eq. (13). The real part of the BCF  $\text{Re}[L(t)]$  involves an infinite sum of real exponentials due to Matsubara contributions. Second, this sum is approximated by a finite set of real exponentials, as originally done in Ref. [68].

We propose a modification to the first step by adopting the more general form Eq. (12). The resulting  $\text{Re}[L(t)]$  again contains an infinite sum [see Eq. (C2)], which we treat using the same second step. Further methodological details are provided in Appendix C.

	Linear	Nonlinear
Time	ESPRIT	GMT&FIT
Fourier	AAA	IP

TABLE I: Classification of the four fitting methods.

Methodologically, these can be classified as shown in Table I. ESPRIT and GMT&FIT operate in the time domain, while AAA and IP work in the frequency domain. ESPRIT and AAA avoid nonlinear parameter dependence by reducing the problem to linear optimization, whereas GMT&FIT and IP rely on nonlinear optimization methods.

Previous assessments of these methods have primarily focused on the reproducibility of the BCF or qualitative features of the dynamics. While quantitative consistency with other methods has been confirmed in Refs. [59, 61], these studies mainly addressed the transient regime. Here, using a harmonic oscillator system, we assess the accuracy of thermalization simulations by direct comparison with exact solutions.

## B. Comparison

We consider spectral densities that scale as a power law at low frequencies and decay exponentially at high frequencies:

$$J(\omega \geq 0) = \frac{\pi}{2} \alpha \omega_c^{1-s} \omega^s e^{-\omega/\omega_c}, \quad (19)$$

where  $\alpha$  is the coupling strength and  $\omega_c$  the cutoff frequency. The exponent  $s$  (Ohmicity) characterizes the low-frequency behavior. This form of spectral density Eq. (19) is widely used, in part because the BCF is analytically available for arbitrary parameters as

$$L(t) = \frac{\alpha \omega_c^2}{2(\beta \hbar \omega_c)^{s+1}} \Gamma(s+1) \times [\zeta(s+1, z^*(t)) + \zeta(s+1, z(t)+1)],$$

with the Gamma function  $\Gamma(s)$ , the Hurwitz zeta function  $\zeta(s, a)$ , and  $z(t) = (1 - i\omega_c t) / (\beta \hbar \omega_c)$ .

Here we focus on the Ohmic spectral density ( $s = 1$ ). The exact solutions can be evaluated with  $\hat{\eta}(s)$  ( $\text{Re}(s) \geq 0$ ) (see Sec. II C), which, in this case, can be expressed in terms of the exponential integrals [see Eqs. (B5) and (B6)]. Since exponential integrals can be computed accurately, this case permits a stringent test of the BCF. In units of  $\hbar = \omega_0 = v_0 = 1$ , we arbitrarily set  $\alpha = 1$ ,  $\omega_c = 10$ , and  $\beta = 1$ . The corresponding BCFs are shown in Figs. 1 (a) and (b).

We construct model BCFs using the four fitting methods introduced in Sec. III A. Data points are sampled equidistantly for both time- and frequency-domain methods. For time-domain methods (ESPRIT and GMT&FIT), we use  $\Delta t_{\text{data}} = 0.01$  over  $t \in [0, t_{\text{max}}]$  with

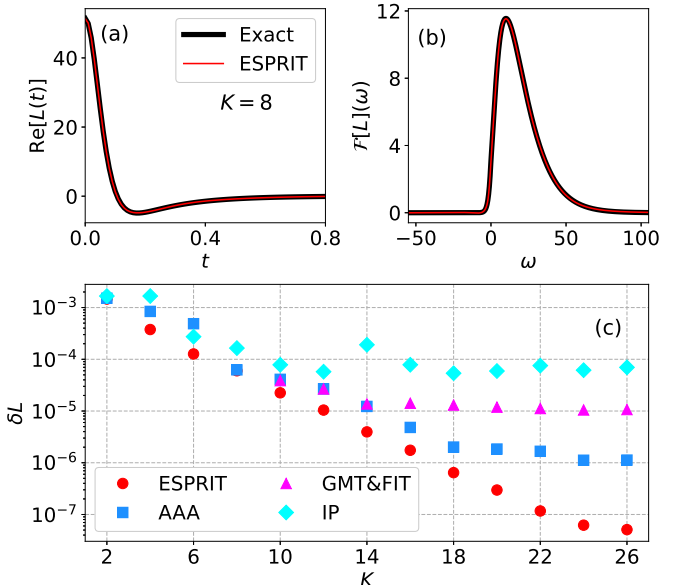


FIG. 1: Error in the model BCF from the four fitting methods. (a), (b): Comparison between the exact BCF (thick black curves) and the ESPRIT results with  $K = 8$  (thin red curves) in the time (a) and frequency (b) domains. All quantities are shown in units of  $\hbar = \omega_0 = v_0 = 1$ . (c): Error  $\delta L$  defined by Eq. (20) as a function of  $K$ .

$t_{\text{max}} = 20$ . For frequency-domain methods (AAA and IP), we use  $\Delta\omega_{\text{data}} = 0.1$  over  $\omega \in [-\omega_{\text{max}}, \omega_{\text{max}}]$  with  $\omega_{\text{max}} = 300$ . In GMT&FIT, we use 8 exponential for fitting the spectral density and  $K - 8$  terms for the Matsubara contribution.

We quantify the relative error in the model BCFs as

$$\delta L \equiv \frac{1}{t_f} \int_0^{t_f} dt \left| \frac{L(t) - L_{\text{mod}}(t)}{L(0)} \right|. \quad (20)$$

Since our main interest lies in simulating thermalization, we set  $t_f = 30$ , corresponding to the time required to reach a steady state (see below). The dependence of  $\delta L$  on  $K$  is shown in Fig. 1 (c). We observe that ESPRIT consistently achieves the lowest error across all values of  $K$ . To illustrate the fitting performance, Figs. 1 (a) and (b) show the ESPRIT results for  $K = 8$  ( $\delta L \simeq 10^{-4}$ ), where the agreement in both time and frequency domains is nearly exact on these scales. AAA and GMT&FIT provide indistinguishable results for  $K = 10, 12$ , and  $14$ . For  $K \geq 16$ , GMT&FIT plateaus, while AAA continues to improve. This suggests that including a mix of decay rates in the model BCF, as done in GMT&FIT, does not significantly enhance accuracy. Lastly, we observe that IP gives the largest error among the methods considered here. This implies that the positivity constraint  $\mathcal{F}[L_{\text{mod}}](\omega) > 0 (\forall \omega)$  may be overly restrictive at the ansatz level.

Using the model BCFs, we compute the dynamics by solving the HEOM Eq. (16). The differential equa-

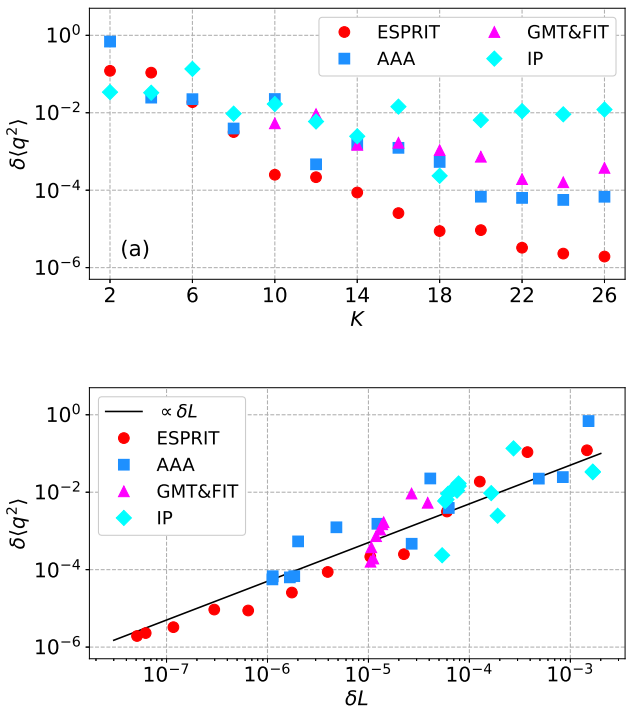


FIG. 2: Error in the steady-state expectation value,  $\delta\langle q^2 \rangle$  defined by Eq. (22), as a function of (a)  $K$  and (b)  $\delta L$ . In (b), the solid black line indicates the linear relation  $\delta\langle q^2 \rangle = 50\delta L$ .

tions are solved by computing the matrix exponential of the generator in the moment representation (see Appendix D 3 for details). Starting from the vacuum state  $\rho_S(0) = |0\rangle\langle 0|$ , we numerically find that the system reaches a steady state at  $t_f = 30$ . The steady-state expectation values can be computed as

$$\langle o^2 \rangle_{\text{mod}} \equiv \text{tr}_S[o^2 \rho_S(t_f)], \quad (21)$$

for  $o = q$  and  $p$ , where the subscript mod indicates evaluation using a model BCF (see Eq. (D7) for the moment representation expression).

We quantify the relative error in the expectation values as

$$\delta\langle o^2 \rangle \equiv \frac{|\langle o^2 \rangle_{\text{eq}} - \langle o^2 \rangle_{\text{mod}}|}{\langle o^2 \rangle_{\text{eq}}}. \quad (22)$$

Since we draw similar conclusions for  $o = q$  and  $p$ , we focus on  $o = q$  in the following. Figure 2 (a) shows the  $K$ -dependence of the error. We observe that it resembles the behavior in Fig. 1 (c), where the error in the model BCF is plotted. Previous work Ref. [51] showed that the error in expectation values can be bounded from above by  $\delta L$ . To clarify this connection, Fig. 2 (b) plots  $\delta\langle q^2 \rangle$  against  $\delta L$ . We find that the trend can be well captured

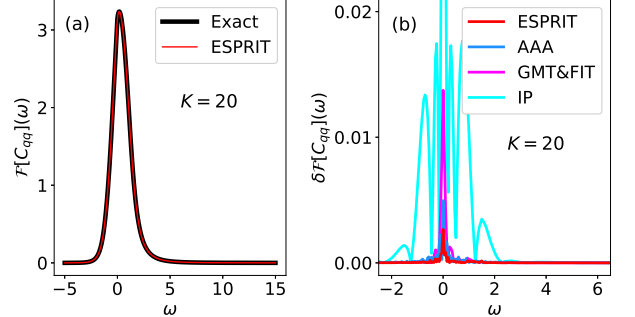


FIG. 3: Error in the autocorrelation function. All dimensional quantities are shown in units of  $\omega_0 = 1$ . (a): Comparison between the exact autocorrelation function (thick black curve) and the ESPRIT result with  $K = 20$  (thin red curve). (b): Relative deviation  $\delta\mathcal{F}[C_{qq}](\omega)$  defined by Eq. (24) for the four fitting methods with  $K = 20$ .

by a linear scaling,  $\delta\langle q^2 \rangle \propto \delta L$ , as indicated by the solid black line in the figure. This scaling is consistent with the analytic bound in the small- $\delta L$  limit in Ref. [51]. However, we note that the bound grows exponentially with time and does not tightly constrain the long-time (steady-state) error.

We next examine the autocorrelation function

$$C_{oo}^{\text{mod}}(t) \equiv \langle \exp(iH_{\text{tot}}^{\times}t/\hbar)(o) o \rangle_{\text{mod}}, \quad (23)$$

(see Eq. (D8) for the moment-representation expression). Its Fourier transform is given by  $\mathcal{F}[C_{oo}^{\text{mod}}](\omega) = 2\text{Re}[\int_0^\infty dt C_{oo}^{\text{mod}}(t) \exp(i\omega t)]$ . We compute the time integral using Simpson's rule with grid spacing  $\Delta t_F = 0.1$ . Figure 3 (a) compares the exact autocorrelation function with the ESPRIT result ( $K = 20$ ), where good agreement is obtained on this scale. To see the error more closely, we plot

$$\delta\mathcal{F}[C_{oo}](\omega) \equiv \frac{|\mathcal{F}[C_{oo} - C_{oo}^{\text{mod}}](\omega)|}{\max_{\omega'} |\mathcal{F}[C_{oo}](\omega')|}, \quad (24)$$

in Fig. 3 (b). Overall, ESPRIT yields the smallest error, while IP results in the largest error, consistent with earlier findings.

### C. Sub-Ohmic case

As a more challenging case, we consider a sub-Ohmic spectral density of the form Eq. (19), with parameters  $s = 0.5$ ,  $\alpha = 1$ ,  $\omega_c = 10$ , and  $\beta = 10$  in units of  $\hbar = \omega_0 = v_0 = 1$ . The resulting BCFs are shown in Figs. 4 (a) and (b). At finite temperatures,  $\mathcal{F}[L](\omega) \simeq 2J(\omega)/(\beta\hbar\omega)$  near  $\omega = 0$  [see Eq. (17)], leading to a divergence at  $\omega = 0$  in sub-Ohmic cases, as seen in Fig. 4 (b). This divergence corresponds to a long tail in  $\text{Re}[L(t)]$ , posing a new challenge absent in the Ohmic case.

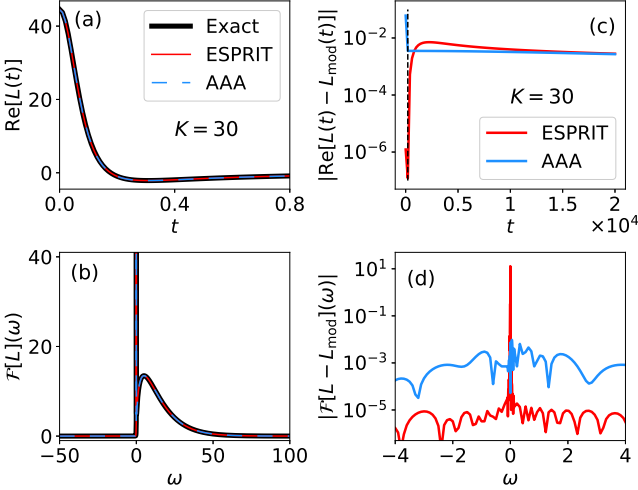


FIG. 4: Error in the model BCF from ESPRIT and AAA with  $K = 30$ . All quantities are shown in units of  $\hbar = \omega_0 = v_0 = 1$ . (a), (b): Comparison between the exact BCF (thick black curves) and the fitted results from ESPRIT (thin red curves) and AAA (thin dashed blue curves) in the (a) time and (b) frequency domains. (c), (d): Error in (c)  $\text{Re}[L_{\text{mod}}(t)]$  and (d)  $\mathcal{F}[L_{\text{mod}}](\omega)$  for ESPRIT (red curve) and AAA (blue curve). In (c), the thin dashed vertical black line shows  $t = 200$ , the fitting range for ESPRIT. In (d), the divergent region near  $\omega = 0$ , where  $\mathcal{F}[L](\omega) > 50$ , is excluded.

Here we examine ESPRIT and AAA. For ESPRIT, data points are sampled equidistantly with  $\Delta t_{\text{data}} = 0.01$  over  $t \in [0, t_{\text{max}}]$ , and we set  $t_{\text{max}} = 200$ . For AAA, which operates in the frequency domain, we treat the regions near  $\omega = 0$  and large  $|\omega|$  separately: data points are equidistantly sampled on a logarithmic scale near  $\omega = 0$  and on a linear scale for large  $|\omega|$ . This strategy captures the divergent behavior of  $\mathcal{F}[L](\omega)$  near  $\omega = 0$  and its smooth variation at large  $|\omega|$ . Further details are provided in Appendix E 1.

In Figs. 4 (a) and (b), we present the fitting results of ESPRIT and AAA with  $K = 30$ , showing good agreement with the exact BCF on these scales. In Ref. [66], AAA was applied to a sub-Ohmic spectral density, but significant deviations in  $\text{Re}[L(t)]$  were reported even at short times. The good agreement in Fig. 4 (a) suggests that this discrepancy is not due to a fundamental limitation of AAA. Instead, the deviation may stem from inadequate data point sampling, which in Ref. [66] was performed logarithmically over the entire frequency range.

In Fig. 4(c), we show the error in  $\text{Re}[L_{\text{mod}}(t)]$  in the long-time region. The thin dashed vertical line shows  $t = t_{\text{max}}$ . ESPRIT yields significantly smaller error for  $t \leq t_{\text{max}}$ , where the fitting is performed. However, the ESPRIT error grows abruptly for  $t > t_{\text{max}}$  and exceeds that of AAA for  $t \gtrsim 800$ , potentially degrading accuracy near  $\omega = 0$  in the frequency domain. This is confirmed in Fig. 4(d), where the ESPRIT error is smaller overall but spikes near  $\omega = 0$ , surpassing the AAA error.

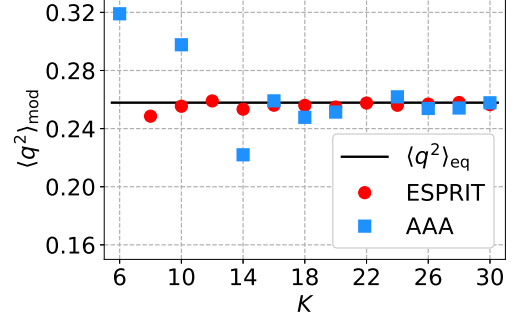


FIG. 5: Comparison of the exact equilibrium expectation value (black line) with the steady-state values obtained with ESPRIT (red circles) and AAA (blue squares) as a function of  $K$ .

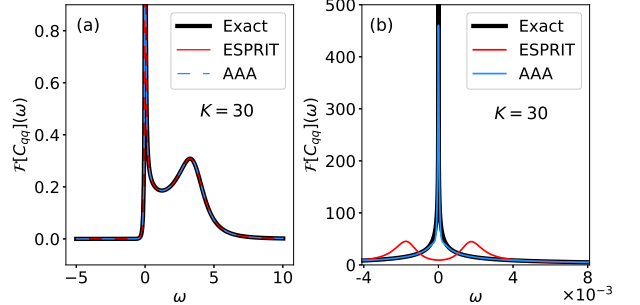


FIG. 6: Comparison between the exact autocorrelation function (thick black curve) and the ESPRIT (thin red curves) and AAA (thin blue curves) results with  $K = 30$ . Panel (b) shows a magnified view around  $\omega = 0$ . All quantities are shown in units of  $\omega_0 = 1$ .

Now we assess how the errors in the model BCFs impact thermalization simulations. To obtain the exact solutions, we numerically compute  $\hat{\eta}(s)$  ( $\text{Re}(s) \geq 0$ ) using Eq. (10) for  $s \in \mathbb{R}_{>0}$  and Eq. (11) for  $\text{Re}(s) = 0$ , where the  $\omega'$ -integral is performed up to  $\omega' = 10^3$  with the SciPy function `scipy.integrate.quad`. The quantities  $\langle q^2 \rangle_{\text{mod}}$  and  $\mathcal{F}[C_{oo}^{\text{mod}}](\omega)$  are computed as described above. We observe convergent results for  $o = q$  with  $t_f = 10^4$  in ESPRIT and  $t_f = 2 \times 10^5$  in AAA. For  $o = p$ , the analysis parallels that of the previously discussed Ohmic case. Thus, our subsequent analysis focuses exclusively on  $o = q$ .

In Fig. 5, we compare the exact equilibrium expectation value  $\langle q^2 \rangle_{\text{eq}}$  with  $\langle q^2 \rangle_{\text{mod}}$  for various  $K$ . We see that the ESPRIT results are notably more stable and accurate for small  $K$ , likely due to the smaller error in the BCF over the region  $t \leq t_{\text{max}}$ . Figure 6 (a) compares the exact autocorrelation function  $\mathcal{F}[C_{qq}](\omega)$  to  $\mathcal{F}[C_{qq}^{\text{mod}}](\omega)$  with  $K = 30$ . The time integral for the Fourier transform is computed as in the Ohmic case. Both AAA and ESPRIT agree closely with the exact result on this scale, including the divergence near  $\omega = 0$  [see Eq. (B3)].

To examine the reproducibility of the divergence more

closely, Fig. 6 (b) shows a zoom around  $\omega = 0$ . We observe that AAA captures the divergent behavior well up to  $\mathcal{F}[C_{qq}](\omega) \simeq 450$ , whereas ESPRIT fails in the region  $\omega \in [-4 \times 10^{-3}, 4 \times 10^{-3}]$ . We confirm that increasing  $K$  yields only marginal improvement. This failure stems from the poor reproduction of  $\text{Re}[L(t)]$  in the long-time region discussed above. As detailed in Appendix E2, extending the fitting range  $t_{\max}$  improves the accuracy of  $\text{Re}[L_{\text{mod}}(t)]$  at long times and yields a better description of the divergent behavior (see Fig. 10). However, since ESPRIT requires equidistant data points together with small grid spacings to resolve short-time features,  $t_{\max}$  is practically limited, thereby constraining the accuracy achievable with ESPRIT.

Exact analysis of a dephasing model revealed non-exponential long-time decoherence [69]. It was argued from this result that methods based on autonomous linear systems (e.g., HEOM and pseudomode), which at most yield polynomial-exponential time dependence, can only approximate dynamics over finite intervals. The divergence of  $\lim_{\omega \rightarrow 0} \mathcal{F}[C_{qq}](\omega)$  signals the non-exponential decay of  $C_{qq}(t)$ . Nevertheless, excellent agreement with AAA is observed in Fig. 6(b), motivating further investigation of complex spectral densities using HEOM and pseudomode method.

#### IV. EXAMPLE: TWO-SPIN SYSTEM

In this section, we describe the procedure for testing a model BCF. Suppose that the total Hamiltonian is given by Eq. (1) with a BCF  $L(t)$ . To obtain the open quantum dynamics, we use a model BCF  $L_{\text{mod}}(t)$  as defined in Eq. (6). To assess its validity, we consider a harmonic oscillator system Eq. (9) with the same BCF. This system contains two free parameters:  $\omega_0$  and  $v_0$ , which are chosen to reflect properties of the original system. Here we propose setting  $\omega_0$  to one of the Bohr frequencies of the effective system Hamiltonian, and choosing  $v_0$  such that the steady-state expectation value of  $V_S^2$  is approximately matched as

$$v_0^2 \langle q^2 \rangle_{\text{eq}} \simeq \lim_{t \rightarrow \infty} \text{tr}_S[V_S^2 \rho_S(t)]. \quad (25)$$

If evaluating the right-hand side is difficult, a representative value for  $V_S^2$  may be used instead. With  $\omega_0$  and  $v_0$  determined in this way, we test  $L_{\text{mod}}(t)$  as performed in the previous section.

As an example, we consider a system of two identical spins with

$$H_{S,\text{eff}} = \frac{\hbar\omega_s}{2}(\sigma_z^{(1)} + \sigma_z^{(2)}) + \hbar g \sum_{i=x,y,z} \sigma_i^{(1)} \sigma_i^{(2)},$$

$$V_S = \sigma_x^{(1)} + \sigma_x^{(2)},$$

where  $\sigma_i^{(n)}$  ( $i = x, y, z$ ) are the Pauli matrices for the  $n$ -th spin ( $n = 1, 2$ ),  $\omega_s$  denotes the energy splitting, and  $g$  is the spin-spin coupling strength. We take the

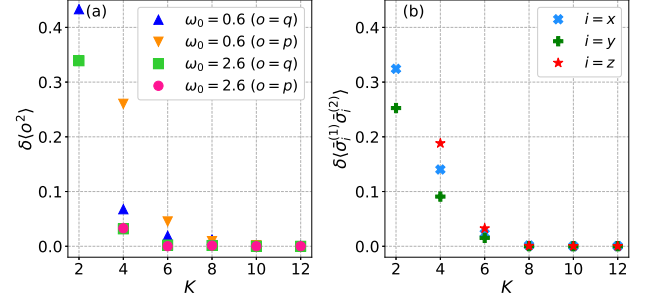


FIG. 7: Error in the steady-state expectation value as a function of  $K$  for (a) the harmonic oscillator system [see Eq. (22)] and (b) two-spin system [see Eq. (26)]

spectral density of the form Eq. (19) with  $s = 1$  and set  $g = 0.4$ ,  $\alpha = 0.2$ ,  $\omega_c = 10$ , and  $\beta = 1$  in units of  $\hbar = \omega_s = 1$ . The model BCF  $L_{\text{mod}}(t)$  is constructed with ESPRIT, using data sampled as in the previous section with  $\Delta t_{\text{data}} = 0.01$  and  $t_{\max} = 20$ . Time evolution is computed by solving the HEOM Eq. (16) using the fourth-order Runge-Kutta method with step size  $dt = 10^{-3}$  and truncation condition  $\rho_j(t) = 0$  for  $\sum_{k=1}^K j_k > 6$ .

The eigenvalues of  $H_{S,\text{eff}}$  are  $-3\hbar g$ ,  $\hbar g \pm \hbar\omega_s$ , and  $\hbar g$ . Setting  $\hbar = \omega_s = 1$  and  $g = 0.4$ , the smallest and largest Bohr frequencies are 0.26 and 2.6, respectively. We thus consider two cases:  $\omega_0 = 0.6$  and  $\omega_0 = 2.6$ . To determine  $v_0$  from Eq. (25), we estimate  $\lim_{t \rightarrow \infty} \text{tr}_S[V_S^2 \rho_S(t)]$  using a model BCF. This procedure yields  $v_0 = 1.2$  for  $\omega_0 = 0.6$  and  $v_0 = 2.1$  for  $\omega_0 = 2.6$ . The exact equilibrium expectation values and autocorrelation functions are then evaluated to test the validity of  $L_{\text{mod}}(t)$ .

We begin by examining the steady-state expectation values. In Fig. 7 (a), we show the  $K$ -dependence of  $\delta\langle o^2 \rangle$  ( $o = q$  and  $p$ ) defined by Eq. (22), where  $\langle o^2 \rangle_{\text{mod}}$  [see Eq. (21)] is computed at  $t_f = 400$  for  $\omega_0 = 0.6$  and  $t_f = 15$  for  $\omega_0 = 2.6$ , starting from the vacuum state  $\rho_S(0) = |0\rangle\langle 0|$ . We find that the error becomes negligible on this scale, corresponding to  $\delta\langle o^2 \rangle < 10^{-2}$ , when  $K \geq 10$  for  $\omega_0 = 0.6$  and  $K \geq 6$  for  $\omega_0 = 2.6$ . This suggests convergence around  $K = 6 - 10$  for the two-spin system. To verify this, we consider the steady-state correlations between the two spins. Let  $\langle o \rangle_K \equiv \text{tr}[o \rho_S(t_f)]$  denote the expectation value computed with  $K$  exponential terms. The spin correlations are then evaluated as  $\langle \bar{\sigma}_i^{(1)} \bar{\sigma}_i^{(2)} \rangle_K$  ( $i = x, y, z$ ) with  $\bar{\sigma}_i^{(n)} = \sigma_i^{(n)} - \langle \sigma_i^{(n)} \rangle_K$  ( $n = 1, 2$ ). We quantify the relative error as

$$\delta\langle \bar{\sigma}_i^{(1)} \bar{\sigma}_i^{(2)} \rangle \equiv \frac{|\langle \bar{\sigma}_i^{(1)} \bar{\sigma}_i^{(2)} \rangle_{K_{\text{ref}}} - \langle \bar{\sigma}_i^{(1)} \bar{\sigma}_i^{(2)} \rangle_K|}{\langle \bar{\sigma}_i^{(1)} \bar{\sigma}_i^{(2)} \rangle_{K_{\text{ref}}}}, \quad (26)$$

using a reference value computed with  $K_{\text{ref}}$ , which we set  $K_{\text{ref}} = 20$ . Figure 7 (b) shows the  $K$ -dependence of  $\delta\langle \bar{\sigma}_i^{(1)} \bar{\sigma}_i^{(2)} \rangle$  ( $i = x, y, z$ ), computed at  $t_f = 30$  with both spins initially in the ground state. We find that

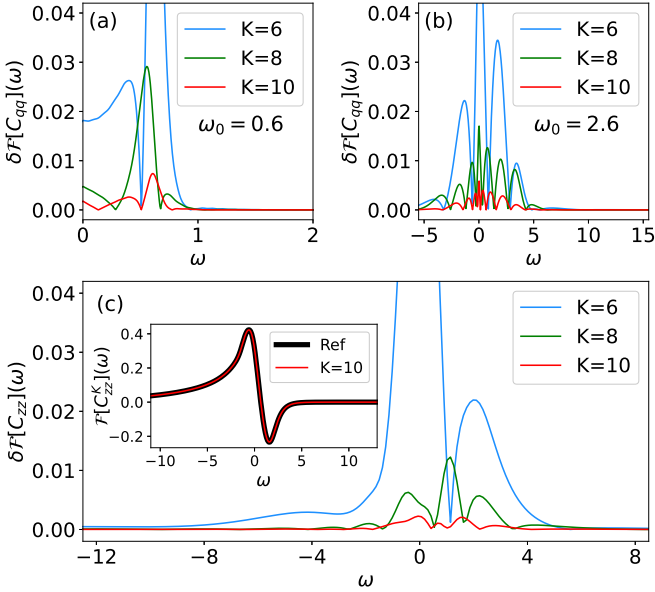


FIG. 8: Error in the correlation functions. All dimensional quantities are shown in units of  $\omega_s = 1$ . (a), (b): Relative deviation from the exact autocorrelation function for the harmonic oscillator system with (a)  $\omega_0 = 0.6$  and (b)  $\omega_0 = 2.6$ . (c): Relative deviation from the reference dynamical correlation function,  $\delta\mathcal{F}[C_{zz}](\omega)$  defined by Eq. (27), for the two-spin system. The inset shows comparison between the reference result ( $K_{\text{ref}} = 20$ ) and the result with  $K = 10$ .

$\delta\langle\bar{\sigma}_i^{(1)}\bar{\sigma}_i^{(2)}\rangle < 10^{-2}$  is achieved for  $K \geq 8$ , consistent with the above estimates from the harmonic oscillator case.

We next examine the correlation function. The time integral for the Fourier transform is computed as in the previous section with grid spacing  $\Delta t_f = 0.01$ . Figures 8 (a) and (b) show the  $K$ -dependence of  $\delta\mathcal{F}[C_{qq}](\omega)$  defined by Eq. (24). The computed results become indistinguishable from the exact ones on a natural scale when  $\delta\mathcal{F}[C_{qq}](\omega) \lesssim 10^{-2}$ . As shown in the figures, this accuracy is achieved with  $K = 10$  for both  $\omega_0 = 0.6$  and  $\omega_0 = 2.6$ . For the two-spin system, we consider dynamical correlation functions defined by  $C_{ii}^K(t) \equiv \langle\sigma_i^{(1)}\exp(iH_{\text{tot}}^X t/\hbar)\sigma_i^{(2)}\rangle_K$ . Within the HEOM framework, it is computed using Eq. (D6). From spin permutation symmetry, we have  $C_{ii}^K(-t) = [C_{ii}^K(t)]^*$ , leading to the Fourier transform:  $\mathcal{F}[C_{ii}^K](\omega) = 2\text{Re}[\int_0^{t_f} dt C_{ii}^K(t)\exp(i\omega t)]$ . We then quantify the error similarly to  $\delta\mathcal{F}[C_{oo}](\omega)$  as

$$\delta\mathcal{F}[C_{ii}](\omega) \equiv \frac{|\mathcal{F}[C_{ii}^{K_{\text{ref}}}] - \mathcal{F}[C_{ii}^K](\omega)|}{\max_{\omega'} |\mathcal{F}[C_{ii}^{K_{\text{ref}}}](\omega')|}, \quad (27)$$

with  $K_{\text{ref}} = 20$ . The error behaves similarly for  $i = x, y$ , and  $z$ , and we plot  $\delta\mathcal{F}[C_{zz}](\omega)$  in Fig. 8 (c). We observe that  $\delta\mathcal{F}[C_{zz}](\omega) < 10^{-2}$  is also achieved with  $K = 10$ , consistent with the harmonic oscillator case. As shown in the inset, the result closely matches the reference.

In summary, we have found that the accuracy of the thermalization simulations can be effectively estimated using surrogate harmonic oscillator systems, supporting the validity of our proposed approach.

## V. CONCLUDING REMARKS

To test the accuracy of dynamics computed using a model BCF, we proposed using a harmonic oscillator system with known exact solutions. We presented several methods to numerically evaluate these solutions for general spectral densities (Sec. II C) and proposed a moment-based representation to simplify the computation (Sec. II D). Applying the testing procedure to a two-spin system, we found that the harmonic oscillator case provides reasonable estimates of the simulation accuracy (Sec. IV).

Using the methodologies introduced in this article, we evaluated the performance of several state-of-the-art methods for efficiently constructing the BCF. For the Ohmic spectral density, we found that ESPRIT, proposed in Ref. [66], achieves the smallest error (Sec. III B). However, we also discussed its potential limitation when applied to sub-Ohmic spectral densities at finite temperatures, where, AAA proposed in Ref. [59], more accurately captures the characteristic divergence of the equilibrium correlation function (Sec. III C).

In addition to the main findings, this study opens up several promising directions for future research. One such direction is the application of the moment representation introduced in Sec. II D to systems involving anharmonic oscillators. Although the truncation is no longer exact in such cases, this representation may still offer computational advantages over the conventional Fock basis, as suggested by a study of an optomeahcnial system with weak anharmonicity [45] and the demonstrated efficiency of HEOM in treating general systems. Another potential direction involves the model BCF given in Eq. (6), which is compatible with the more general form  $v_k(t) = t^{n_k} e^{-z_k t}$ , where  $n_k \in \mathbb{Z}_{\geq 0}$  and  $z_k \in \mathbb{C}$ . The exponential ansatz Eq. (15) corresponds to the special case  $n_k = 0$ . This generalized form has been shown to be effective for describing low-temperature baths [70, 71]. The analysis in Sec. III B implies that methods reducing the problem to linear optimization tend to outperform brute-force nonlinear optimization approaches. These insights motivate the development of a new method capable of efficiently handling the cases with  $n_k > 0$ .

## Acknowledgments

I thank Yoshitaka Tanimura for his valuable input throughout the research. I am also grateful to Shoki Koyanagi, Jianshu Cao, Michael Thoss, and Johannes Feist for fruitful discussions. This work was supported by JSPS KAKENHI Grant Number JP23KJ1157.

## Appendix A: Pseudomode method

In this appendix, we discuss the pseudomode method, where the open quantum dynamics Eq. (3) are described by embedding the system into an extended space with auxiliary bosonic modes (pseudomodes). While early works [24–27] assumed the extended state evolves under a Gorini-Kossakowski-Sudarshan-Lindblad (GKSL) equation [72, 73], the framework remains applicable even when the evolution is not completely positive [44, 74] or Hermitian-preserving [68, 75, 76]. As noted in Ref. [25], non-GKSL master equations offer greater flexibility in modeling BCFs.

As recently shown in Refs. [43–45], the key difference between the pseudomode method and the HEOM is the use of a moment-based representation (see Appendix D for details) for the auxiliary state. To illustrate this, consider a GKSL master equation with  $Q$  pseudomodes:

$$\begin{aligned} \frac{d}{dt}\varrho(t) = & \\ -\frac{i}{\hbar}\left(H_S + \sum_{k,k'=1}^Q \hbar\omega_{k,k'}a_k^\dagger a_{k'} + V_S X_{ps}\right)^\times \varrho(t) & \quad (\text{A1}) \\ + \sum_{k=1}^Q \kappa_k \mathcal{D}[a_k](\varrho(t)), \end{aligned}$$

where  $\varrho(t)$  is the density operator in the extended space,  $a_k$  ( $a_k^\dagger$ ) is the annihilation (creation) operator for the  $k$ -th pseudomode, the interaction operator  $X_{ps}$  is assumed to be  $X_{ps} = \sum_{k=1}^Q g_k(a_k + a_k^\dagger)$ , and  $\mathcal{D}[a_k](\varrho) = a_k\varrho a_k^\dagger - (a_k^\dagger a_k\varrho + \varrho a_k^\dagger a_k)/2$  is the dissipator. The fitting parameters are  $\omega_{k,k'} (= \omega_{k',k}) \in \mathbb{R}$ ,  $g_k \in \mathbb{R}$ , and  $\kappa_k \in \mathbb{R}_{>0}$ . The internal dynamics of the pseudomodes is governed by  $\mathfrak{L}_{ps} = -i\sum_{k,k'=1}^Q \omega_{k,k'}(a_k^\dagger a_{k'})^\times + \sum_{k=1}^Q \kappa_k \mathcal{D}[a_k]$ , where the vacuum state  $|\mathbf{0}\rangle$  is a steady state  $\mathfrak{L}_{ps}(|\mathbf{0}\rangle\langle\mathbf{0}|) = 0$ . Assuming the initial state  $\varrho(0) = \rho_S(0)|\mathbf{0}\rangle\langle\mathbf{0}|$ , the model BCF corresponding to Eq. (A1) reads as [26]

$$\begin{aligned} L_{\text{mod}}(t \geq 0) \equiv & \frac{1}{\hbar} \text{tr} [X_{ps} e^{\mathfrak{L}_{ps} t} (X_{ps} |\mathbf{0}\rangle\langle\mathbf{0}|)] \\ = & \frac{1}{\hbar} \mathbf{g}^\top e^{-i\tilde{\omega}t} \mathbf{g}, \end{aligned} \quad (\text{A2})$$

with  $\mathbf{g}^\top = [g_1, \dots, g_Q]$ , and  $\tilde{\omega}_{k,k'} = \omega_{k,k'} - (i/2)\delta_{k,k'}\kappa_k/2$ .

In Appendix D, we explore the moment representation of the oscillator system state. On the other hand, here we consider the moment representation of the pseudomode state. In this case, the map representing the transformation, Eq. (D2), is defined as [44]

$$\mathcal{T} \equiv e^{\sum_{k=1}^Q a_k^L (a_k^\dagger)^R},$$

which operates trivially on the system state space. Let  $\varphi(t) = \mathcal{T}(\varrho(t))$ . With the aid of Eq. (D4), operating  $\mathcal{T}$

on Eq. (A1) yields the evolution equation for  $\varphi(t)$  as

$$\begin{aligned} \frac{d}{dt}\varphi(t) = & -\frac{i}{\hbar}H_S^\times\varphi(t) \\ -i\sum_{k,k'=1}^Q \tilde{\omega}_{k,k'}a_k^\dagger a_{k'}\varphi(t) + i\sum_{k,k'=1}^Q \tilde{\omega}_{k,k'}^*\varphi(t)a_k^\dagger a_{k'} \\ -\frac{i}{\hbar}\sum_{k=1}^Q g_k \left[ V_S^L(a_k^\dagger\varphi(t)) - V_S^R(\varphi(t)a_k) \right] \\ -\frac{i}{\hbar}\sum_{k=1}^Q g_k V_S^\times \left( a_k\varphi(t) + \varphi(t)a_k^\dagger \right). \end{aligned}$$

Reducing the pseudomode degrees of freedom by taking the matrix element as  $\varphi_{\mathbf{m},\mathbf{n}}(t) \equiv \langle \mathbf{m} | \varphi(t) | \mathbf{n} \rangle$ , we find

$$\begin{aligned} \frac{d}{dt}\varphi_{\mathbf{m},\mathbf{n}}(t) = & -\frac{i}{\hbar}H_S^\times\varphi_{\mathbf{m},\mathbf{n}}(t) \\ -i\sum_{k,k'=1}^Q \tilde{\omega}_{k,k'} \sqrt{m_k(m_{k'} + 1 - \delta_{k,k'})} \varphi_{\mathbf{m}-\mathbf{e}_k+\mathbf{e}_{k'},\mathbf{n}}(t) \\ + i\sum_{k,k'=1}^Q \tilde{\omega}_{k,k'}^* \sqrt{n_k(n_{k'} + 1 - \delta_{k,k'})} \varphi_{\mathbf{m},\mathbf{n}-\mathbf{e}_k+\mathbf{e}_{k'}}(t) \\ -\frac{i}{\hbar}\sum_{k=1}^Q g_k \left[ \sqrt{m_k} V_S^L \varphi_{\mathbf{m}-\mathbf{e}_k,\mathbf{n}}(t) - \sqrt{n_k} V_S^R \varphi_{\mathbf{m},\mathbf{n}-\mathbf{e}_k}(t) \right] \\ -\frac{i}{\hbar}\sum_{k=1}^Q g_k V_S^\times \left( \sqrt{m_k + 1} \varphi_{\mathbf{m}+\mathbf{e}_k,\mathbf{n}}(t) \right. \\ \left. + \sqrt{n_k + 1} \varphi_{\mathbf{m},\mathbf{n}+\mathbf{e}_k}(t) \right). \end{aligned}$$

These equations are in fact a special case of the HEOM Eq. (8) with

$$\boldsymbol{\theta} = i \begin{bmatrix} \mathbf{g} \\ \mathbf{g} \end{bmatrix}, \quad \mathbf{v}(0) = -\frac{i}{\hbar} \begin{bmatrix} \mathbf{g} \\ \mathbf{g} \end{bmatrix},$$

$$D = \begin{bmatrix} I & O \\ O & O \end{bmatrix}, \quad \bar{D} = \begin{bmatrix} O & O \\ O & I \end{bmatrix},$$

and

$$Z = \begin{bmatrix} i\tilde{\omega} & O \\ O & -i\tilde{\omega}^* \end{bmatrix},$$

with the  $Q \times Q$  identity matrix  $I$  and zero matrix  $O$ . From Eq. (6), the model BCF corresponding to these is given by

$$L_{\text{mod}}(t) = \frac{1}{\hbar} \begin{bmatrix} \mathbf{g} \\ \mathbf{0} \end{bmatrix}^\top \begin{bmatrix} e^{-i\tilde{\omega}t} & O \\ O & e^{i\tilde{\omega}^*t} \end{bmatrix} \begin{bmatrix} \mathbf{g} \\ \mathbf{g} \end{bmatrix},$$

which is consistent with Eq. (A2). In summary, we show that the HEOM are obtained by expressing the pseudomode equation in the moment representation.

In Sec. III A, we introduce the interacting pseudomode approach to a model BCF. The ansatz Eq. (18) is obtained by setting  $\mathbf{g} = \sqrt{\hbar/(2\pi)} \mathbf{l}$  in Eq. (A2). In Ref. [77], the interaction between the pseudomodes is restricted to the nearest-neighbor ones for efficient simulations using the tensor-network state [78]. The fully interacting pseudomodes were considered in Refs. [60, 61] and we focus on this approach as it offers greater flexibility in modelling BCFs. In Sec. III A, we use the open source package available in Ref. [79] to determine the parameters.

## Appendix B: Exact solutions for the harmonic oscillator system

In this appendix, we present the explicit formulas of the exact solutions for the harmonic oscillator system.

### 1. Solution of the Heisenberg equation of motion

It is instructive to start with the solution of the Heisenberg equation of motion. With Eqs. (1), (2), and (9), we find that  $q(t) \equiv \exp(iH^\times t/\hbar)(q)$  satisfies

$$\begin{aligned} \frac{d^2}{dt^2}q(t) + \frac{1}{M} \int_0^t ds \eta(t-s) \frac{d}{ds}q(s) + \omega_0^2 q(t) \\ = -\frac{1}{Mv_0} X_B^0(t) - \frac{\eta(t)}{M} q, \end{aligned}$$

with  $X_B^0(t) = \exp(iH_B^\times t/\hbar)(X_B)$ ,  $M = \hbar/(\omega_0 v_0^2)$ , and  $\eta(t) = (2/\pi) \int_0^\infty d\omega (J(\omega)/\omega) \cos(\omega t)$ . We see from this equation of motion that  $\omega_0$  represents the effective frequency of the oscillator and  $\eta(t)$  represents the friction coefficient. This equation can be solved using, for instance, the Laplace transform [80]. The general solution is given by

$$\begin{aligned} q(t) = q \frac{d}{dt} G_+(t) + p \omega_0 G_+(t) \\ - \frac{1}{Mv_0} \int_0^t ds G_+(t-s) X_B^0(s), \end{aligned} \quad (B1)$$

where  $G_+(t)$ , which is defined in the Laplace space as

$$\begin{aligned} \hat{G}_+(s) &\equiv \int_0^\infty dt G_+(t) e^{-st} \\ &= \frac{1}{\omega_0^2 + s^2 + s\hat{\eta}(s)/M}, \end{aligned} \quad (B2)$$

with  $\hat{\eta}(s) = \int_0^\infty dt \eta(t) e^{-st}$ , is the solution of the differential equation

$$\frac{d^2}{dt^2} G_+(t) + \frac{1}{M} \int_0^t ds \eta(t-s) \frac{d}{ds} G_+(s) + \omega_0^2 q(t) = 0$$

with initial conditions  $G_+(0) = 0$  and  $(d/dt)G_+(0) = 1$ .

## 2. Analytic solutions

Using the path integral formulation, the authors of Ref. [17] found analytic expressions of the equilibrium expectation values  $\langle o^2 \rangle_{\text{eq}}$  and autocorrelation functions  $C_{oo}(t)$  for  $o = q$  and  $p$  (see Sec. II C for their definitions). First, the equilibrium expectation values are given by

$$\langle q^2 \rangle_{\text{eq}} = \frac{1}{\beta \hbar \omega_0} \sum_{n=-\infty}^{\infty} \frac{\omega_0^2}{\omega_0^2 + \nu_n^2 + \zeta_n},$$

and

$$\langle p^2 \rangle_{\text{eq}} = \frac{1}{\beta \hbar \omega_0} \sum_{n=-\infty}^{\infty} \frac{\omega_0^2 + \zeta_n}{\omega_0^2 + \nu_n^2 + \zeta_n},$$

with  $\nu_n = 2\pi n/(\beta \hbar)$  and  $\zeta_n = \nu_n \hat{\eta}(\nu_n)/M$ . Second, the equilibrium autocorrelation functions in the frequency domain are given by

$$\mathcal{F}[C_{qq}](\omega) = \frac{2\omega_0}{1 - e^{-\beta \hbar \omega}} \text{Im}[\hat{G}_+(-i\omega)]$$

with  $\hat{G}_+(-i\omega) = [\omega_0^2 - \omega^2 - i\omega \hat{\eta}(-i\omega)/M]^{-1}$  (see Eq. (B2)), and

$$\mathcal{F}[C_{pp}](\omega) = \left( \frac{\omega}{\omega_0} \right)^2 \mathcal{F}[C_{qq}](\omega).$$

Note that the zero temperature limit can be obtained by replacing the infinite sum with the integral for  $\langle o^2 \rangle_{\text{eq}}$  and the factor  $1/(1 - \exp(-\beta \hbar \omega))$  with the step function for  $\mathcal{F}[C_{oo}](\omega)$ .

We examine the behavior of  $\mathcal{F}[C_{qq}](\omega)$  in the vicinity of  $\omega = 0$  for different Ohmilities. Inserting Eq. (11) into Eq. (B2) yields

$$\begin{aligned} \text{Im}[\hat{G}_+(-i\omega)] = \\ \frac{J(\omega)/M}{(\omega^2 - \omega_0^2 + \omega \text{Im}[\hat{\eta}(-i\omega)]/M)^2 + (J(\omega)/M)^2}, \end{aligned}$$

with  $\text{Im}[\hat{\eta}(-i\omega)]$  involves the Cauchy principal value. Assuming  $\lim_{\omega \rightarrow 0^+} \omega \text{Im}[\hat{\eta}(-i\omega)] = 0$ , which is numerically confirmed for the cases discussed in this article, the denominator becomes  $\omega_0^4$  in the limit  $\omega \rightarrow 0^+$ . This leads to  $\lim_{\omega \rightarrow 0^+} \text{Im}[\hat{G}_+(-i\omega)] = J(\omega)/(M\omega_0^4)$ . Assuming  $J(\omega \simeq 0^+) = \mathcal{J} \omega^s$  near  $\omega = 0$ , we thus find at finite temperatures

$$\mathcal{F}[C_{qq}](\omega \simeq 0^+) = \frac{2\mathcal{J}}{\beta} \left( \frac{v_0}{\hbar \omega_0} \right)^2 \omega^{s-1}.$$

This indicates that  $\mathcal{F}[C_{qq}](\omega)$  in the vicinity of  $\omega = 0$  is sensitive to the Ohmicity as

$$\lim_{\omega \rightarrow 0} \mathcal{F}[C_{qq}](\omega) \begin{cases} = \infty & (0 < s < 1), \\ > 0 & (s = 1), \\ = 0 & (s > 1). \end{cases} \quad (B3)$$

Similar behavior is expected for different systems. Recently, Ref. [81] proposed a machine learning approach to infer Ohmicity from the time evolution of a system observable. However, this method may be difficult to implement experimentally, as it relies on assumptions, such as an initially factorized state, that are not easily verified in laboratory. Given that linear response functions like  $\mathcal{F}C_{qq}$  are experimentally accessible, Eq. (B3) might offer a more practical alternative for identifying Ohmicity.

### 3. Cases with analytic $\hat{\eta}(s)$

The above formulas indicate that we only need  $\hat{\eta}(|s|)$  ( $|s| > 0$ ) to evaluate the equilibrium expectation values and  $\hat{\eta}(-i\omega)$  ( $\omega \in \mathbb{R}$ ) for the equilibrium autocorrelation functions. Combining these two, we need  $\hat{\eta}(s)$  ( $\text{Re}(s) \geq 0$ ) to evaluate the exact solutions. Here we present analytic expressions of this quantity for several spectral densities.

One example is the generalized Mayer-Tannor form Eq. (C1) (see Appendix C for details). In this case,  $\eta(t)$  is given by a sum of exponential functions [see Eq. (12)] and the integral for the Laplace transform  $\hat{\eta}(s) = \int_0^\infty dt \eta(t) \exp(-st)$  yields

$$\hat{\eta}(s) = -2i \sum_j \left[ \frac{c_j}{\mu_j(s + \mu_j)} - \frac{c_j^*}{\mu_j^*(s + \mu_j^*)} \right], \quad (\text{B4})$$

for  $\text{Re}(s) \geq 0$ .

The other example is the Ohmic spectral density with the exponential cutoff:

$$J(\omega \geq 0) = \frac{\pi}{2} \alpha \omega e^{-\omega/\omega_c}.$$

Using the formulas Eqs. (10) and (11), we find

$$\hat{\eta}(|s|) = -\alpha \text{Im} \left[ E(i|s|/\omega_c) e^{i|s|/\omega_c} \right], \quad (\text{B5})$$

for  $|s| > 0$  and

$$\begin{aligned} \hat{\eta}(-i\omega) &= \frac{\pi}{2} \alpha e^{-|\omega|/\omega_c} \\ &+ i \frac{\alpha}{2} \left[ E(\omega/\omega_c) e^{\omega/\omega_c} - E(-\omega/\omega_c) e^{-\omega/\omega_c} \right]. \end{aligned} \quad (\text{B6})$$

for  $\omega \in \mathbb{R}$ , where  $E(s)$  is the exponential integral defined by

$$E(z) = \text{p.v.} \int_0^\infty dx \frac{e^{-(x+z)}}{x+z}.$$

This can be evaluated, for instance, using the SciPy functions `scipy.linalg.exp1` for  $z \in \mathbb{C} \wedge z \notin \mathbb{R}_{\leq 0}$  and `scipy.linalg.expi` for  $z \in \mathbb{R}_{<0}$ .

### Appendix C: Generalized Mayer-Tannor (GMT) decomposition

In this appendix, we explore the generalized Mayer-Tannor decomposition introduced in Eq. (12). The spectral density is given by the Fourier transform of the imaginary part,  $J(\omega) \equiv i\mathcal{F}[\text{Im}(L)](\omega)$ , and reads as

$$J(\omega) = \sum_j \frac{4\omega \text{Im}(c_j(\omega^2 + (\mu_j^*)^2))}{[(\omega + \Omega_j)^2 + \Gamma_j^2] \cdot [(\omega - \Omega_j)^2 + \Gamma_j^2]}. \quad (\text{C1})$$

Using this, we can derive  $\text{Re}[L(t)]$  as

$$\begin{aligned} \text{Re}[L(t \geq 0)] &= 2 \sum_j \text{Im} \left[ c_j \cot \left( \frac{\beta \hbar \mu_j}{2} \right) e^{-\mu_j t} \right] \\ &+ \frac{2}{\beta \hbar} \sum_{n=1}^{\infty} i J(i\nu_n) e^{-\nu_n t}. \end{aligned} \quad (\text{C2})$$

with  $\nu_n = 2\pi n / (\beta \hbar)$ . The terms in the second line represent the Matsubara contribution.

In Sec. II C, we propose leveraging this decomposition to accurately compute the exact values of  $\langle o^2 \rangle_{\text{eq}}$  and  $\mathcal{F}[C_{oo}](\omega)$ . These quantities can be computed from the complex parameters  $\{c_j, \mu_j\}_j$  using Eq. (B4). One way to obtain the parameters  $\{c_j, \mu_j\}_j$  is by fitting  $\text{Im}[L(t \geq 0)]$  with the ESPRIT algorithm (see Sec. III A). Although the algorithm does not inherently enforce the constraints  $\text{Im}[L(t)] \in \mathbb{R}$  and  $J(\omega \geq 0) \geq 0$ , we expect these conditions to be satisfied if the fitting of  $\text{Im}[L(t)]$  is sufficiently accurate.

In Sec. III A, we introduce the Generalized Mayer-Tannor with FITted Matsubara modes (GMT&FIT) to construct a model BCF  $L_{\text{mod}}(t)$ . This two-step approach involves fitting  $J(\omega)$  and  $\text{Re}[L(t)]$ . In Sec. III B, we apply ESPRIT to fit  $\text{Im}[L(t \geq 0)]$ , which yields  $J(\omega)$  as Eq. (C1). The resulting complex parameters  $\{c_j, \mu_j\}_j$  define  $\text{Re}[L(t)]$  as Eq. (C2), which includes the infinite Matsubara sum. To approximate the Matsubara contribution using a finite number of real exponentials, we adopt the ansatz

$$\begin{aligned} \text{Re}[L_{\text{mod}}(t \geq 0)] &= 2 \sum_j \text{Im} \left[ c_j \cot \left( \frac{\beta \hbar \mu_j}{2} \right) e^{-\mu_j t} \right] \\ &+ \sum_n b_n^{\text{MT}} e^{-\gamma_n^{\text{MT}} t}. \end{aligned}$$

with real fitting parameters  $\{b_n^{\text{MT}}, \gamma_n^{\text{MT}}\}_n$  constrained by  $\gamma_n^{\text{MT}} > 0$ . We determine these using the SciPy function `scipy.optimize.minimize` with the 'L-BFGS-M' method. The initial guess is set to  $b_n^{\text{MT}} = 2iJ(i\nu_n) / (\beta \hbar)$  and  $\gamma_n^{\text{MT}} = \nu_n$  motivated by Eq. (C2).

## Appendix D: Moment representation

### 1. Introduction

In this appendix, we explore the moment representation of the oscillator system state. The moment representation of  $\rho_j$  (omitting the time argument for now) is introduced in Eq. (14):

$$\phi_{m,n,j} = \frac{\text{tr}_S(a^m \rho_j (a^\dagger)^n)}{\sqrt{m! n!}}. \quad (\text{D1})$$

Let  $\phi_j \equiv \sum_{m,n=0}^{\infty} \phi_{m,n,j} |m\rangle\langle n|$ , with which  $\{\phi_{m,n,j}\}_{m,n=0}^{\infty}$  can be obtained from its matrix elements as  $\phi_{m,n,j} = \langle m|\phi_j|n\rangle$ . The map  $\mathcal{T}$  transforming  $\rho_j$  to  $\phi_j$ ,  $\phi_j \equiv \mathcal{T}(\rho_j)$ , is linear and is given by

$$\mathcal{T} = \sum_{n=0}^{\infty} \frac{[a^L (a^\dagger)^R]^n}{n!} = e^{a^L (a^\dagger)^R}, \quad (\text{D2})$$

where the superscripts  $L$  and  $R$  represent the operation from the left and right, respectively, as introduced below Eq. (4). This indicates that the inverse  $\mathcal{T}^{-1}$ , which describes the inverse transformation  $\rho_j \equiv \mathcal{T}^{-1}(\phi_j)$ , is given by  $\mathcal{T}^{-1} = \exp(-a^L (a^\dagger)^R)$ . We can show

$$\text{tr}_S(o) = \langle 0|\mathcal{T}(o)|0\rangle, \quad (\text{D3})$$

and

$$\begin{aligned} \mathcal{T}(ao) &= a\mathcal{T}(o), \quad \mathcal{T}(a^\dagger o) = a^\dagger \mathcal{T}(o) + \mathcal{T}(o)a^\dagger, \\ \mathcal{T}(oa^\dagger) &= \mathcal{T}(o)a^\dagger, \quad \mathcal{T}(oa) = a\mathcal{T}(o) + \mathcal{T}(o)a, \end{aligned} \quad (\text{D4})$$

for any system operators  $o$ .

### 2. HEOM in the moment representation

The expression of the HEOM Eq. (8) in the moment representation can be derived by applying  $\mathcal{T}$  and using Eq. (D4). Inserting Eqs. (2) and (9), we find

$$\begin{aligned} \frac{d}{dt} \phi_j(t) &= -\frac{i}{\hbar} \mathcal{T}[H_S^\times \rho_j(t)] - \sum_{k,k'=1}^K Z_{k,k'}^j \phi_{j-e_k+e_{k'}}(t) \\ &+ v_0 \sum_{k=1}^K \sqrt{j_k} ([D\mathbf{v}(0)]_k \mathcal{T}[q\rho_{j-e_k}] - [\bar{D}\mathbf{v}(0)]_k \mathcal{T}[\rho_{j-e_k}q]) \\ &- \frac{v_0}{\hbar} \sum_{k=1}^K \theta_k \sqrt{j_k + 1} \mathcal{T}[q^\times \rho_{j+e_k}], \end{aligned} \quad (\text{D5})$$

with

$$\begin{aligned} \mathcal{T}[H_S^\times \rho_j(t)] &= (\hbar\omega_0 + \lambda v_0^2)(a^\dagger a)^\times \phi_j(t) \\ &+ \lambda v_0^2 \left[ \frac{1}{2}(a^\dagger)^2 \phi_j(t) - \frac{1}{2} \phi_j(t) a^2 + a^\dagger \phi_j(t) a^\dagger - a \phi_j(t) a \right], \end{aligned}$$

$$\mathcal{T}[q\rho_{j-e_k}(t)] = q\phi_{j-e_k}(t) + \frac{1}{\sqrt{2}}a\phi_{j-e_k}(t)a^\dagger,$$

$$\mathcal{T}[\rho_{j-e_k}(t)q] = \phi_{j-e_k}(t)q + \frac{1}{\sqrt{2}}a\phi_{j-e_k}(t)a,$$

and

$$\mathcal{T}[q^\times \rho_{j+e_k}(t)] = \frac{1}{\sqrt{2}}(a^\dagger \phi_{j+e_k}(t) - \phi_{j+e_k}(t)a).$$

Taking the matrix element, we see that  $(d/dt)\phi_{m,n,j}(t)$  with depth  $\mathcal{H} \equiv m + n + \sum_{k=1}^K j_k$  depends only on elements  $\phi_{m',n',j'}(t)$  with depth  $m' + n' + \sum_{k=1}^K j'_k = \mathcal{H}$  or  $\mathcal{H} - 2$ . For example, the last line of Eq. (D5) involves  $\phi_{m-1,n,j+e_k}(t)$  and  $\phi_{m,n-1,j+e_k}(t)$  for  $k = 1, 2, \dots, K$ , both with depth  $\mathcal{H}$ . This structure ensures that elements  $\{\phi_{m,n,j}\}$  with depth  $\leq \mathcal{H}$  are decoupled from those with greater depth. This enables exact truncation in computing their evolution.

### 3. Computation of $\langle o^2 \rangle_{\text{mod}}$ and $C_{oo}^{\text{mod}}(t)$

Here we present the way of computing  $\langle o^2 \rangle_{\text{mod}}$  Eq. (21) and  $C_{oo}^{\text{mod}}(t)$  Eq. (23) within the HEOM framework in the original and moment representations. To this end, we introduce the orthonormal vector notation of the auxiliary states as  $\rho \equiv \sum_j \rho_j |j\rangle$ , with  $(j|j') = \delta_{j,j'}$ . The HEOM Eq. (8) can then be expressed as  $(d/dt)\rho(t) = \mathcal{L}(\rho(t))$  with the linear generator  $\mathcal{L}$ . Due to the linearity, its formal solution is given by  $\rho(t) = \exp(\mathcal{L}t)(\rho(0))$ , where the initial state reads as  $\rho(0) = \rho_S(0)|0\rangle$  [see the discussion below Eq. (8)]. We can then evaluate the quantities as

$$\langle o^2 \rangle_{\text{mod}} = \text{tr}_S [(\mathbf{0}|(o^2)^L e^{\mathcal{L}t_f}(\rho(0))],$$

and

$$C_{oo}^{\text{mod}}(t) = \text{tr}_S [(\mathbf{0}|o^L e^{\mathcal{L}t} (o^L e^{\mathcal{L}t_f}(\rho(0))))]. \quad (\text{D6})$$

A similar expression in the moment representation can be obtained by  $\phi = \mathcal{T}(\rho)$ , where  $\mathcal{T}$  operates trivially on the auxiliary state space. The evolution equation for  $\rho(t)$  yields  $(d/dt)\phi(t) = \mathfrak{M}(\phi(t))$  with  $\mathfrak{M} = \mathcal{T}\mathcal{L}\mathcal{T}^{-1}$ , which corresponds to the HEOM in the moment representation Eq. (D5). The initial state is given by  $\phi(0) = \mathcal{T}(\rho_S(0))|0\rangle$ . With the initial vacuum state  $\rho_S(0) = |0\rangle\langle 0|$ , for instance, we have  $\mathcal{T}(\rho_S(0)) = |0\rangle\langle 0|$ .

Using Eq. (D3), the above formulas for  $\langle o^2 \rangle_{\text{mod}}$  and  $C_{oo}^{\text{mod}}(t)$  can be transformed to the moment representation expression as

$$\langle o^2 \rangle_{\text{mod}} = \langle 0|(\mathbf{0}|(o^2)^L e^{\mathfrak{M}t_f}(\phi(0))|0\rangle, \quad (\text{D7})$$

and

$$C_{oo}^{\text{mod}}(t) = \langle 0|(\mathbf{0}|o^L e^{\mathfrak{M}t} (o^L e^{\mathfrak{M}t_f}(\phi(0))))|0\rangle. \quad (\text{D8})$$

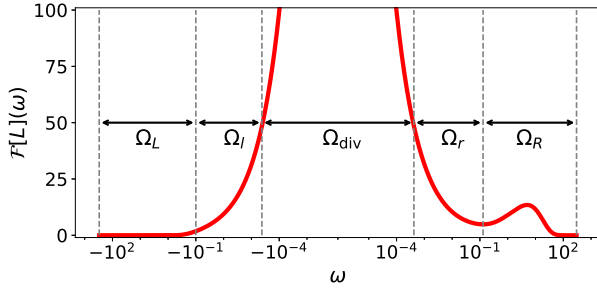


FIG. 9: Partitioning of the frequency space into five subregions for frequency-domain fitting.

In these equations, we have introduced  $\mathcal{O} \equiv \mathcal{T}\mathcal{O}\mathcal{T}^{-1}$  for  $\mathcal{O} = (o^2)^L$  and  $o^L$ , where the explicit expressions can be found using Eq. (D4). These are the second-order moments of the ladder operators. Therefore, the truncation at the depth  $\mathcal{H} = 2$  (setting  $\phi_{m,n,j} = 0$  for  $m+n+\sum_{k=1}^K j_k > 2$ ) is sufficient to compute them.

Throughout this article, we evaluate Eqs. (D7) and (D8) by computing the matrix exponentiation  $\exp(\mathfrak{M}t)$  using the SciPy function `scipy.sparse.linalg.expm` to avoid time discretization errors.

#### Appendix E: Supplemental information for the sub-Ohmic case

In this appendix, we provide supplemental information for the accuracy analysis of the sub-Ohmic case discussed in Sec. III C.

##### 1. Choice of data points for AAA

We begin by discussing the choice of data points for AAA. Unlike the Ohmic case (Sec. III B), the selection must account for the divergence of  $\mathcal{F}[L](\omega)$  at  $\omega = 0$  [see Fig. 4 (b)]. Our goal is to capture both the divergent behavior near  $\omega = 0$  and the smooth behavior at large  $|\omega|$ . To achieve this, we divide the frequency space  $\Omega \equiv [-\omega_{\max}, \omega_{\max}]$  (with  $\omega_{\max} = 300$ ) into five subspaces as shown in Fig. 9. Two outer regions,  $\Omega_L$  and  $\Omega_R$ , cover the smooth tails. Two intermediate regions,  $\Omega_l$  and  $\Omega_r$ , capture the sharp rise near  $\omega = 0$ . The central region,  $\Omega_{\text{div}}$ , contains the divergence at  $\omega = 0$ .

To prevent divergence in the fitting procedure, we exclude  $\Omega_{\text{div}}$ . In the smooth regions  $\Omega_L$  and  $\Omega_R$ , data points are sampled equidistantly with  $\Delta\omega_{\text{data}} = 0.1$ . In  $\Omega_l$  and  $\Omega_r$ , we adopt a finer log-scale grid. Let  $\Omega_r \equiv [\omega_r^{(0)}, \omega_r^{(1)}]$  ( $0 < \omega_r^{(0)} < \omega_r^{(1)}$ ) and  $\Omega_l \equiv [\omega_l^{(1)}, \omega_l^{(0)}]$  ( $\omega_l^{(1)} < \omega_l^{(0)} < 0$ ). In each region  $\Omega_s$  ( $s = r$  and  $l$ ), we sample  $N$  points  $\{\omega_{s,n}\}_{n=0}^{M-1}$  as

$$\log |\omega_{s,n}| = \log |\omega_s^{(0)}| + \frac{n}{N-1} \left( \log |\omega_s^{(1)}| - \log |\omega_s^{(0)}| \right).$$

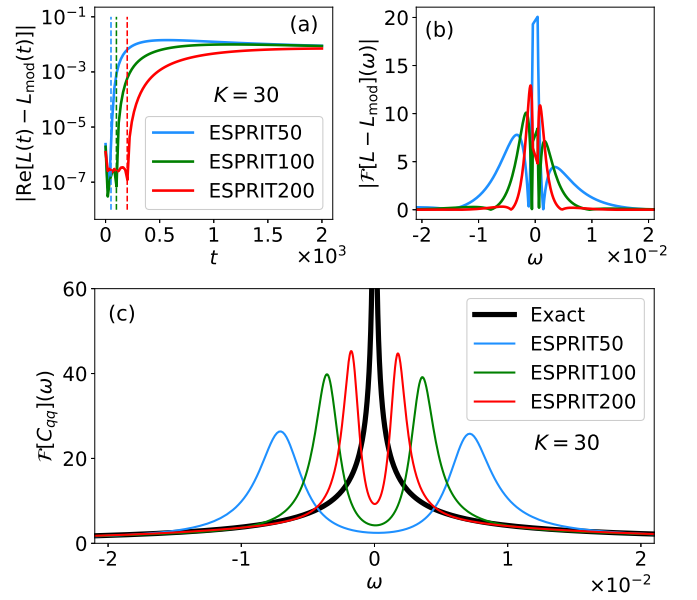


FIG. 10: Dependence of ESPRIT fitting quality with  $K = 30$  on  $t_{\max}$ . All quantities are shown in units of  $\hbar = \omega_0 = v_0 = 1$ . (a), (b): Error in (a)  $\text{Re}[L_{\text{mod}}(t)]$  and (b)  $\mathcal{F}[L_{\text{mod}}](\omega)$  for  $t_{\max} = 50$  (blue curve), 100 (green curve), and 200 (red curve). In (a), the thin dashed vertical lines show  $t = t_{\max}$ . In (b), the divergent region near  $\omega = 0$ , where  $\mathcal{F}[L](\omega) > 50$ , is excluded. (c): Comparison between the exact autocorrelation function (thick black curve) and the ESPRIT results (thin colored curves).

We set  $N = 100$ , which is one order of magnitude smaller than the number of data points in the smooth regions. The endpoints  $\omega_s^{(0)}$  are chosen such that  $\mathcal{F}[L](\omega) \leq 50$ , yielding  $\omega_r^{(0)} = 4.2161 \times 10^{-4}$  and  $\omega_l^{(0)} = -4.1881 \times 10^{-4}$ . The inner boundaries of the smooth regions  $\omega_s^{(1)}$  are arbitrarily set to  $\omega_r^{(1)} = 0.13$  and  $\omega_l^{(1)} = -0.1$ .

##### 2. $t_{\max}$ -dependence for ESPRIT

We next discuss how the ESPRIT results depend on  $t_{\max}$  by comparing cases with  $t_{\max} = 50$ , 100, and 200 (the analysis in Sec. III C uses  $t_{\max} = 200$ ). All computations use  $K = 30$ , and we verify that larger  $K$  values do not significantly affect the results. Figure 10 (a) shows the error in  $\text{Re}[L_{\text{mod}}](t)$  in the long-time region. As expected, we see that the accuracy improves with increasing  $t_{\max}$  increases. Figure 10 (b) shows the error in  $\mathcal{F}[L_{\text{mod}}](\omega)$  near  $\omega = 0$ . Although the largest error does not decrease monotonically with increasing  $t_{\max}$ , the frequency range captured accurately becomes narrower as  $t_{\max}$  increases.

We examine the reproducibility of the autocorrelation function. First, we confirm that all values of  $t_{\max}$  show good agreement on the scale of Fig. 6 (a) (not shown).

Figure 10 (c) compares the exact autocorrelation function with the ESPRIT results near  $\omega = 0$ . Consistent with the improvements seen in Figs. 10 (a) and (b), larger  $t_{\max}$

values more accurately capture the divergent behavior near  $\omega = 0$ .

---

[1] C. Schinabeck, R. Härtle, and M. Thoss, Hierarchical quantum master equation approach to electronic-vibrational coupling in nonequilibrium transport through nanosystems: Reservoir formulation and application to vibrational instabilities, *Phys. Rev. B* **97**, 235429 (2018).

[2] Y. Tanimura, Numerically “exact” approach to open quantum dynamics: The hierarchical equations of motion (HEOM), *J. Chem. Phys.* **153**, 020901 (2020).

[3] Lachlan P. Lindoy, Arkajit Mandal, and David R. Reichman, Quantum dynamical effects of vibrational strong coupling in chemical reactivity, *Nat Commun* **14**, 2733 (2023).

[4] Veljko Janković, Holstein polaron transport from numerically “exact” real-time quantum dynamics simulations, *J. Chem. Phys.* **159**, 094113 (2023).

[5] Stefanie Hilt, Saroosh Shabbir, Janet Anders, and Eric Lutz, Landauer’s principle in the quantum regime, *Phys. Rev. E* **83**, 030102(R) (2011).

[6] M. Perarnau-Llobet, H. Wilming, A. Riera, R. Gallego, and J. Eisert, Strong Coupling Corrections in Quantum Thermodynamics, *Phys. Rev. Lett.* **120**, 120602 (2018).

[7] Peter Talkner and Peter Hänggi, Colloquium: Statistical mechanics and thermodynamics at strong coupling: Quantum and classical, *Rev. Mod. Phys.* **92**, 041002 (2020).

[8] Shoki Koyanagi and Yoshitaka Tanimura, Classical and quantum thermodynamics described as a system–bath model: The dimensionless minimum work principle, *J. Chem. Phys.* **160**, 234112 (2024).

[9] Shoki Koyanagi and Yoshitaka Tanimura, Classical and quantum thermodynamics in a nonequilibrium regime: Application to thermostatic Stirling engine, *J. Chem. Phys.* **161**, 114113 (2024).

[10] R. P. Feynman and F. L. Vernon Jr., The theory of a general quantum system interacting with a linear dissipative system, *Ann. Phys.* **24**, 118 (1963).

[11] P. Ullersma, An exactly solvable model for Brownian motion: I. Derivation of the Langevin equation, *Physica* **32**, 27–55 (1966).

[12] A. O. Caldeira and A. J. Leggett, Quantum tunnelling in a dissipative system, *Ann. Phys.* **149**, 374 (1983).

[13] G. W. Ford, J. T. Lewis, and R. F. O’Connell, Quantum Langevin equation, *Phys. Rev. A* **37**, 4419 (1988).

[14] U. Weiss, *Quantum Dissipative Systems* (World Scientific, Singapore, 2008).

[15] S. Chandrasekhar, Stochastic Problems in Physics and Astronomy, *Rev. Mod. Phys.* **15**, 1 (1943).

[16] A. S. Trushechkin, M. Merkli, J. D. Cresser, and J. Anders, Open quantum system dynamics and the mean force Gibbs state, *AVS Quantum Sci.* **4**, 012301 (2022).

[17] Hermann Grabert, Peter Schramm, and Gert-Ludwig Ingold, Quantum Brownian motion: The functional integral approach, *Physics Reports* **168**, 115 - 207 (1988).

[18] Yoshitaka Tanimura, Reduced hierarchical equations of motion in real and imaginary time: Corre-  
lated initial states and thermodynamic quantities, *J. Chem. Phys.* **141**, 044114 (2014).

[19] Shoki Koyanagi (private communication).

[20] Yoshitaka Tanimura and Ryogo Kubo, Time Evolution of a Quantum System in Contact with a Nearly Gaussian-Markoffian Noise Bath, *J. Phys. Soc. Jpn.* **58**, 101 (1989).

[21] Yun-an Yan, Fan Yang, Yu Liu, and Jiushu Shao, Hierarchical approach based on stochastic decoupling to dissipative systems, *Chem. Phys. Lett.* **395**, 216 (2004).

[22] Akihito Ishizaki and Yoshitaka Tanimura, Quantum Dynamics of System Strongly Coupled to Low-Temperature Colored Noise Bath: Reduced Hierarchy Equations Approach, *J. Phys. Soc. Jpn.* **74**, 3131 (2005).

[23] Y. Tanimura, Stochastic Liouville, Langevin, Fokker-Planck, and Master Equation Approaches to Quantum Dissipative Systems, *J. Phys. Soc. Jpn.* **75**, 082001 (2006).

[24] A. Imamoglu, Stochastic wave-function approach to non-Markovian systems, *Phys. Rev. A* **50**, 3650 (1994).

[25] B. M. Garraway, Nonperturbative decay of an atomic system in a cavity, *Phys. Rev. A* **55**, 2290 (1997).

[26] Dario Tamascelli, Andrea Smirne, Susana F. Huelga, and Martin B. Plenio, Non-perturbative treatment of non-Markovian dynamics of open quantum systems, *Phys. Rev. Lett.* **120**, 030402 (2018).

[27] A. Smirne, D. Tamascelli, J. Lim, M.B. Plenio, and S.F. Huelga, Non-perturbative treatment of open-system multi-time expectation values in Gaussian bosonic environments, *Open Systems & Information Dynamics* **29**, 2250019 (2022).

[28] Nancy Makri and Dmitrii E. Makarov, Tensor propagator for iterative quantum time evolution of reduced density matrices. I. Theory, *J. Chem. Phys.* **102**, 4600–4610 (1995).

[29] Nancy Makri and Dmitrii E. Makarov, Tensor propagator for iterative quantum time evolution of reduced density matrices. II. Numerical methodology, *J. Chem. Phys.* **102**, 4611–4618 (1995).

[30] A. Strathearn, P. Kirton, D. Kilda, J. Keeling, and B. W. Lovett, Efficient non-Markovian quantum dynamics using time-evolving matrix product operators, *Nat Commun* **9**, 3322 (2018).

[31] Mathias R. Jørgensen and Felix A. Pollock, Exploiting the Causal Tensor Network Structure of Quantum Processes to Efficiently Simulate Non-Markovian Path Integrals, *Phys. Rev. Lett.* **123**, 240602 (2019).

[32] Gerald E. Fux, Piper Fowler-Wright, Joel Beckles, Eoin P. Butler, Paul R. Eastham, Dominic Gribben, Jonathan Keeling, Dainius Kilda, Peter Kirton, Ewen D.C. Lawrence, Brendon W. Lovett, Eoin O’Neill, Aidan Strathearn, and Roosmarijn de Wit, OQuPy: A Python package to efficiently simulate non-Markovian open quantum systems with process tensors, *J. Chem. Phys.* **161**, 124108 (2024).

[33] Valentin Link, Hong-Hao Tu, and Walter

T. Strunz, Open Quantum System Dynamics from Infinite Tensor Network Contraction, *Phys. Rev. Lett.* **132**, 200403 (2024).

[34] M. H. Beck, A. Jäckle, G. A. Worth, and H.-D. Meyer, The multiconfiguration time-dependent Hartree (MCTDH) method: a highly efficient algorithm for propagating wavepackets, *Phys. Rep.* **324**, 1 (2000).

[35] Haobin Wang and Michael Thoss, Multilayer formulation of the multiconfiguration time-dependent Hartree theory, *J. Chem. Phys.* **119**, 1289–1299 (2003).

[36] Alex W. Chin, Ángel Rivas, Susana F. Huelga, and Martin B. Plenio, Exact mapping between system-reservoir quantum models and semi-infinite discrete chains using orthogonal polynomials, *J. Math. Phys.* **51**, 092109 (2010).

[37] Javier Prior, Alex W. Chin, Susana F. Huelga, and Martin B. Plenio, Efficient Simulation of Strong System-Environment Interactions, *Phys. Rev. Lett.* **105**, 050404 (2010).

[38] D. Tamascelli, A. Smirne, J. Lim, S. F. Huelga, and M. B. Plenio, Efficient Simulation of Finite-Temperature Open Quantum Systems, *Phys. Rev. Lett.* **123**, 090402 (2019).

[39] Thibaut Lacroix, Brieuc Le Dé, Angela Riva, Angus J. Dunnett, and Alex W. Chin, MPSDynamics.jl: Tensor network simulations for finite-temperature (non-Markovian) open quantum system dynamics, *J. Chem. Phys.* **161**, 084116 (2024).

[40] Jürgen T. Stockburger and C. H. Mak, Stochastic Liouvillian algorithm to simulate dissipative quantum dynamics with arbitrary precision, *J. Chem. Phys.* **110**, 4983–4985 (1999).

[41] L. Diósi, N. Gisin, and W. T. Strunz, Non-Markovian quantum state diffusion, *Phys. Rev. A* **58**, 1699 (1998).

[42] Richard Hartmann and Walter T Strunz, Exact Open Quantum System Dynamics Using the Hierarchy of Pure States (HOPS), *J. Chem. Theory Comput.* **13**, 5834 (2017).

[43] Valentin Link, Kai Müller, Rosaria G. Lena, Kimmo Luoma, François Damanet, Walter T. Strunz, and Andrew J. Daley, Non-Markovian Quantum Dynamics in Strongly Coupled Multimode Cavities Conditioned on Continuous Measurement, *PRX Quantum*, **3**, 020348 (2022).

[44] Meng Xu, Vasilii Vadimov, Malte Krug, J. T. Stockburger, and J. Ankerhold, A Universal Framework for Quantum Dissipation:Minimally Extended State Space and Exact Time-Local Dynamics, *arXiv:2307.16790* [quant-ph].

[45] Masaaki Tokieda, Moment expansion method for composite open quantum systems including a damped oscillator mode, *Phys. Rev. A* **109**, 062228 (2024).

[46] J. Feist, A. I. Fernández-Domínguez, and F. J. García-Vidal, Macroscopic QED for quantum nanophotonics: emitter-centered modes as a minimal basis for multiemitter problems, *Nanophotonics* **10**, 477 (2020).

[47] Seiji Ueno and Yoshitaka Tanimura, Modeling and Simulating the Excited-State Dynamics of a Systemwith Condensed Phases: A Machine Learning Approach *J. Chem. Theory Comput.* **17**, 3618 (2021).

[48] Kiyoto Nakamura and Joachim Ankerhold, Gate operations for superconducting qubits and non-Markovianity, *Phys. Rev. Research* **6**, 033215 (2024).

[49] Nicola Lorenzoni, Thibaut Lacroix, James Lim, Dario Tamascelli, Susana F. Huelga, and Martin B. Plenio, Full Microscopic Simulations Uncover Persistent Quantum Effects in Primary Photosynthesis, *arXiv:2503.17282* [physics.chem-ph].

[50] F. Mascherpa, A. Smirne, S. F. Huelga, and M. B. Plenio Open Systems with Error Bounds: Spin-Boson Model with Spectral Density Variations, *Phys. Rev. Lett.* **118**, 100401 (2017).

[51] Zhen Huang, Lin Lin, Gunhee Park, Yuanran Zhu, Unified analysis of non-Markovian open quantum systems in Gaussian environment using superoperator formalism, *arXiv:2411.08741* [quant-ph]

[52] H.-P. Breuer and F. Petruccione, *The Theory of Open Quantum Systems*, (Oxford University Press, New York, 2002).

[53] Yoshitaka Tanimura, Real-time and imaginary-time quantum hierachal Fokker-Planck equations, *J. Chem. Phys.* **142**, 144110 (2015).

[54] Shoki Koyanagi and Yoshitaka Tanimura, Thermodynamic quantum Fokker-Planck equations and their application to thermostatic Stirling engine, *J. Chem. Phys.* **161**, 112501 (2024).

[55] Tatsushi Ikeda and Gregory D. Scholes, Generalization of the hierarchical equations of motion theory for efficient calculations with arbitrary correlation functions, *J. Chem. Phys.* **152**, 204101 (2020).

[56] Markus Schröder, Michael Schreiber, and Ulrich Kleinekathöfer, Reduced dynamics of coupled harmonic and anharmonic oscillators using higher-order perturbation theory, *J. Chem. Phys.* **126**, 114102 (2007).

[57] Christoph Meier and David J. Tannor, Non-Markovian evolution of the density operator in the presence of strong laser fields, *J. Chem. Phys.* **111**, 3365 (1999).

[58] Y. Nakatsukasa, O. Sète, and L. N. Trefethen, The AAA algorithm for rational approximation, *SIAM J. Sci. Comput.* **40**, A1494–A1522 (2018).

[59] Meng Xu, Yaming Yan, Qiang Shi, J. Ankerhold, and J. T. Stockburger, Taming Quantum Noise for Efficient Low Temperature Simulations of Open Quantum Systems, *Phys. Rev. Lett.* **129**, 230601 (2022).

[60] Ivan Medina, Francisco J. García-Vidal, Antonio I. Fernández-Domínguez, and Johannes Feist, Few-Mode Field Quantization of Arbitrary Electromagnetic Spectral Densities, *Phys. Rev. Lett.* **126**, 093601 (2021).

[61] Maksim Lednev, Francisco J. García-Vidal, and Johannes Feist, Lindblad Master Equation Capable of Describing Hybrid Quantum Systems in the Ultrastrong Coupling Regime, *Phys. Rev. Lett.* **132**, 106902 (2024).

[62] L. Diósi and L. Ferrialdi, General Non-Markovian Structure of Gaussian Master and Stochastic Schrödinger Equations, *Phys. Rev. Lett.* **113**, 200403 (2014).

[63] Neill Lambert, Mauro Cirio, Jhen-dong Lin, Paul Menczel, Pengfei Liang, and Franco Nori, Fixing detailed balance in ancilla-based dissipative state engineering, *Phys. Rev. Research* **6**, 043229 (2024).

[64] Ke Sun, Mingyu Kang, Hanggai Nuomin, George Schwartz, David N. Beratan, Kenneth R. Brown, and Jungsang Kim, Quantum Simulation of Spin-Boson Models with Structured Bath, *arXiv:2405.14624* [quant-ph]

[65] Daniel Potts and Manfred Tasche, Parameter estimation for nonincreasing exponentialsums by Prony-like methods, *Linear Algebra Appl.* **439**, 1024–1039 (2013).

[66] Hideaki Takahashi, Samuel Rudge, Christoph Kaspar, Michael Thoss, Raffaele Borrelli, High accu-

racy exponential decomposition of bath correlation functions for arbitrary and structured spectral densities: Emerging methodologies and new approaches, *J. Chem. Phys.* **160**, 204105 (2024).

[67] Brieuc Le Dé, Amine Jaouadi, Etienne Mangaud, Alex W. Chin, and Michèle Desouter-Lecomte, Managing Temperature in Open Quantum Systems Strongly Coupled with Structured Environments, *J. Chem. Phys.* **160**, 244102 (2024).

[68] Neill Lambert, Shahnawaz Ahmed, Mauro Cirio, and Franco Nori, Modelling the ultra-strongly coupled spin-boson model with unphysical modes, *Nature Communications* **10**, 3721 (2019).

[69] Anton Trushechkin, Long-term behaviour in an exactly solvable model of pure decoherence and the problem of Markovian embedding, *Mathematics* **12**, 1 (2024).

[70] Lei Cui, Hou-Dao Zhang, Xiao Zheng, Rui-Xue Xu, and YiJing Yan, Highly efficient and accurate sum-over-poles expansion of Fermi and Bose functions at near zero temperatures: Fano spectrum decomposition scheme, *J. Chem. Phys.* **151**, 024110 (2019).

[71] Hou-Dao Zhang, Lei Cui, Hong Gong, Rui-Xue Xu, Xiao Zheng, and YiJing Yan Hierarchical equations of motion method based on Fano spectrum decomposition for low temperature environments, *J. Chem. Phys.* **152**, 064107 (2020).

[72] V. Gorini, A. Kossakowski, and E. C. G. Sudarshan, Completely positive dynamical semigroups of N-level systems, *J. Math. Phys.* **17**, 821 (1976).

[73] G. Lindblad, On the Generators of Quantum Dynamical Semigroups, *Commun. Math. Phys.* **48**, 119 (1976).

[74] Gunhee Park, Zhen Huang, Yuanran Zhu, Chao Yang, Garnet Kin-Lic Chan, and Lin Lin, Quasi-Lindblad pseudomode theory for open quantum systems, *Physical Review B* **110**, 195148 (2024).

[75] Si Luo, Neill Lambert, Pengfei Liang, and Mauro Cirio, Quantum-Classical Decomposition of Gaussian Quantum Environments: A Stochastic Pseudomode Model, *PRX Quantum* **4**, 030316 (2023).

[76] Paul Menczel, Ken Funo, Mauro Cirio, Neill Lambert, and Franco Nori, Non-Hermitian Pseudomodes for Strongly Coupled Open Quantum Systems: Unravelings, Correlations and Thermodynamics, *Phys. Rev. Research* **6**, 033237 (2024).

[77] F. Mascherpa, A. Smirne, A. D. Somoza, P. Fernández-Acebal, S. Donadi, D. Tamascelli, S. F. Huelga, and M. B. Plenio, Optimized auxiliary oscillators for the simulation of general open quantum systems, *Phys. Rev. A* **101**, 052108 (2020).

[78] Alejandro D. Somoza, Oliver Marty, James Lim, Susana F. Huelga, and Martin B. Plenio, Dissipation-Assisted Matrix Product Factorization, *Phys. Rev. Lett.* **123**, 100502 (2019).

[79] Johannes Feist, [https://github.com/jfeist/spectral\\_density\\_fit](https://github.com/jfeist/spectral_density_fit)

[80] C. H. Fleming, Albert Roura, and B. L. Hu, Exact analytical solutions to the master equation of quantum Brownian motion for a general environment, *Ann. Phys.* **326**, 1207 (2011).

[81] Jessica Barr, Giorgio Zicari, Alessandro Ferraro, and Mauro Paternostro, Jessica Barr, Giorgio Zicari, Alessandro Ferraro, Spectral density classification for environment spectroscopy, *Mach. Learn.: Sci. Technol.* **5**, 015043 (2024).